Okhotsk Sea and Polar Oceans Research

Volume 4 (2020)

Okhotsk Sea and Polar Oceans Research Association

Mombetsu City, Hokkaido, Japan

Vol. 4

General Information for OSPOR

(July 2019)
* Changed for Vol. 4, 2020

1. Aims and Scope

Okhotsk Sea and Polar Oceans Research (OSPOR) is published by the Okhotsk Sea and Polar Oceans Research Association (OSPORA).

Since 1986 the Okhotsk Sea and Cold Ocean Research Association (OSCORA) has held the International Symposium at Mombetsu, Hokkaido, in Japan every February and has released its proceedings over 30 years. In 2017 OSCORA changed to OSPORA, because the Symposium scope was broadened to include the polar oceans (the Arctic and Antarctic Oceans), the Arctic passages, global warming, and environmental change in Polar Regions.

OSPORA started a reviewed papers system from the 2017 Symposium. The papers are refereed by multiple reviewers, published in the proceedings of the Symposium with a title of “Article”, and opened on the OSPOR web site.

2. Subjects covered by OSPOR

1) Environment of Okhotsk Sea
2) Meteorology and oceanography in polar regions
3) Cold region engineering
4) Arctic sea routes
5) Global warming and environment change
6) Remote sensing
7) Snow, ice and human life
8) Other topics about Okhotsk Sea and Polar Oceans

3. Editorial Policy of OSPOR*

We intend to publish three types of papers;

1) **Article**, containing original scientific materials and results, not submitted for publication elsewhere,
2) **Review**, containing an overview of previous activities, projects and workshops with an outlook of a specific category.

Each of them will be peer-reviewed.

4. Editorial Board

Period: August 2018 - August 2020

5. OSPOR website*

Temporal website: http://okhotsk-mombetsu.jp/okhsympo/top-index.html
E-mail: momsys@o-tower.co.jp

Okhotsk Sea and Polar Oceans Research (OSPOR)

Contents

Volume 4 (2020)

Okhotsk Sea and Polar Oceans Research 4 (2020) 1-9

Article

Storm–mediated ocean–atmosphere heat exchange over the Arctic Ocean: A case study of a Barents Sea cyclone observed in January 2011

Atsuyoshi MANDA[1], Taku MITSUI[2], Jun INOUE[2, 3], Masatake E. HORI[3, 4], Kazuaki KAWAMOTO[5] and Kensuke K. KOMATSU[1]

[1] *Mie University*, *Tsu*, *Japan*
[2] *The Graduate University for Advanced Studies*, *SOKENDAI*, *Tachikawa*, *Japan*
[3] *National Institute of Polar Research, Tachikawa*, *Japan*
[4] *Japan Agency for Marine-Earth Science and Technology*, *Yokosuka, Japan*
[5] *Nagasaki University*, *Nagasaki*, *Japan*

(Received September 9, 2019; Revised manuscript accepted November 19, 2019)

Abstract

Recent studies indicated the importance of cyclones in terms of Arctic warming. Most previous literature has focused on horizontal latent and sensible heat transport from lower latitudes and paid little attention to the effect of surface evaporation in the Arctic Ocean. We here examine the effects of surface evaporation on the lifecycle of a cyclone and thermodynamic structure around a cyclone by conducting a series of numerical simulations, carefully validated with shipboard surface meteorological observations and atmospheric soundings. Although the atmospheric environment and development mechanism of the cyclone are quite different from those of tropical cyclone, the surface fluxes play a role in the life cycle of the cyclone. Enhanced surface evaporation over the Nordic Seas contributes to the longevity of the cyclone, and the effect of evaporation is comparable to that of the surface sensible heat flux. An increase in moisture due to surface evaporation results in atmospheric warming in the lower troposphere over the Barents Sea, mainly because of local condensational and boundary layer heating, and the advection of warm air, which is presumably caused by modification of the air mass around the cyclone. The recent sea-ice decline and associated enhanced evaporation potentially intensify such storm-mediated atmospheric heat-exchange and lead to further Arctic warming.

Key words: cyclone; Barents Sea; air–sea interaction; surface heat flux; Arctic amplification

1. Introduction

Cyclones are an important component of the Arctic climate system (Serreze, 1995). They crucially affect the energy balance of the polar region by transporting huge amounts of heat and moisture (Zahn et al., 2018). In some extreme cases, intense cyclones generate large anomalous warming over the Arctic (e.g., Moore, 2016). Cyclones also affect the concentration and melting of sea ice (Boisvert et al., 2016) and thus control the atmospheric energy supply from the surface. Hence, any changes in cyclone activity directly affect the Arctic energy balance (Zahn et al., 2018).

A recent study showed a coherent interannual variation of moisture transport from lower latitudes and air temperature during winter (Hao et al., 2019). Dufour (2016) showed that transient eddies provide the bulk of the imported mid-latitude moisture (~90% at 70°N), which suggests the importance of cyclones in recent Arctic warming. Meanwhile, surface fluxes play an important role in Arctic warming, especially in the lower troposphere (Screen et al., 2010; Deser et al., 2010; Dai et al., 2019). Strong winds over the ice-free ocean surface associated with cyclones can intensify surface fluxes, which affects the lifecycle of cyclones and in turn atmospheric warming. Adakudlu and Barstad (2011) documented that their modelled cyclone had a prolonged phase of a surface low at its peak intensity when they removed sea ice around Svalbard. Kolstad et al. (2016) showed that surface heat fluxes intensify the mature phase of a polar low and warming in the lower troposphere. Such storm-mediated ocean–atmosphere heat exchange was suggested by Inoue and Hori (2011). However, its detailed process has not been fully examined and is thus not yet fully understood.

In January 2011, we made shipboard atmospheric soundings and surface meteorological observations in the Barents Sea and successfully observed a marine cyclone, which remained around the sea-ice edge in the Barents Sea and may have affected the atmospheric

thermodynamic structure. The present study elucidates the effect of surface evaporation on the lifecycle of this cyclone and the storm-mediated heat exchange process through a series of numerical simulations. Although surface evaporation is not large over the Arctic Ocean, compared to lower latitudes, it has a long-term increasing trend (Boisvert et al., 2015), and the results of the present study will thus shed light on recent Arctic warming and contribute to its future projection.

The remainder of the paper is organized as follows. The data and method used in the study are described in Section 2. Section 3 documents the results of numerical simulations. A summary and discussion are provided in Section 4.

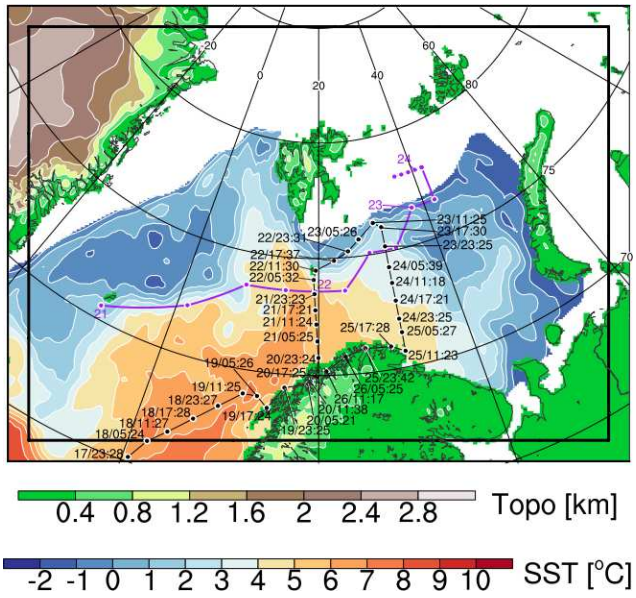

Fig. 1 Map showing the topography (Topo) and SST field derived from OISST on 21 January 2011 in the study area. Overlaid on the SST field are black lines and circles, respectively indicating ship transects and locations of shipboard sounding stations. Numerals with slashes and colons indicate the day of the month and the UTC time (e.g., 21/12:15 represents 12:15 UTC on 21 January 2011) of the sounding. Purple lines with circles represent the tracks of the cyclone estimated from ERA-Interim data; two-digit numbers indicate the day of the month (time is 00:00 UTC). The rectangle with thick black lines marks the domain of the numerical simulations.

2. Data and method

2.1 In situ observations

A joint survey of the Arctic ocean–atmosphere system was conducted by the Japan Agency for Marine–Earth Science and Technology and the Institute of Marine Research in Norway from 13 to 26 January 2011 on board the research vessel (R/V) Johan Hjort of the Institute of Marine Research. Figure 1 shows the locations of sounding stations overlaid on the sea-surface temperature (SST) field. For brevity, we abbreviate times as the day of the month in January 2011 and the UTC time, such that 21/12:15 represents 12:15 UTC on 21 January 2011. On board the ship, we used radiosondes (Vaisala RS92-SGPD) to measure air temperature, relative humidity (RH), and wind velocity every 1 s from the sea surface to approximately 15 km above the sea surface. Surface marine meteorological observations of the SST, surface air temperature (SAT), sea-level pressure (SLP), surface wind velocity, and RH were available at 1-min intervals. We used WindObserver II (Gill Instruments) for surface wind velocity, PTB220 (Vaisala) for SLP, HMP45D (Vaisala) for SAT and RH, SBE-3 (Sea-Bird Electronics) for SST. These in situ data were neither assimilated into the reanalysis dataset nor used in the numerical simulations. They were considered as independent data and used to evaluate the model performance in reproducing atmospheric fields during the survey.

2.2 Atmospheric model

We conducted numerical simulations to elucidate the roles of surface evaporation in the lifecycle of the observed cyclone and atmospheric warming. Version 3.5.1 of the polar-optimized Weather Research and Forecasting model (Polar WRF) developed by Hines and Bromwich (2008) was used in the simulations. Readers are referred to Skamarock et al. (2008) for the specifications of an original version of the model. The land surface model has been optimized for the Arctic climate and well validated using various observational data (Hines and Bromwich, 2008). The model domain is indicated by the rectangle with thick black lines in Figure 1. The horizontal grid spacing was set to 10 km and the model had 50 vertical levels up to 10 hPa. We used five parameterization schemes: the Morrison two-moment scheme (Morrison et al., 2009) for cloud microphysics, Mellor–Yamada–Nakanishi–Niino scheme (Nakanishii and Niino, 2009) for turbulence closure, new Kain–Fritsch scheme (Kain, 2004) for cumulus convection, Dudhia shortwave scheme (Dudhia 1989), and a rapid radiative transfer model (Mlawer et al., 1997) for radiation. The Yonsei University scheme (Hong et al., 2006) was also tested, but the model output varied little for different parametrizations. Optimum Interpolation Sea Surface Temperature (OISST; Reynolds et al., 2007) data were used for the bottom boundary condition over the sea surface. European centre for medium-range weather forecasts interim reanalysis (ERA-Interim; Dee et al. 2011) was employed for the initial and boundary conditions of other prognostic variables.

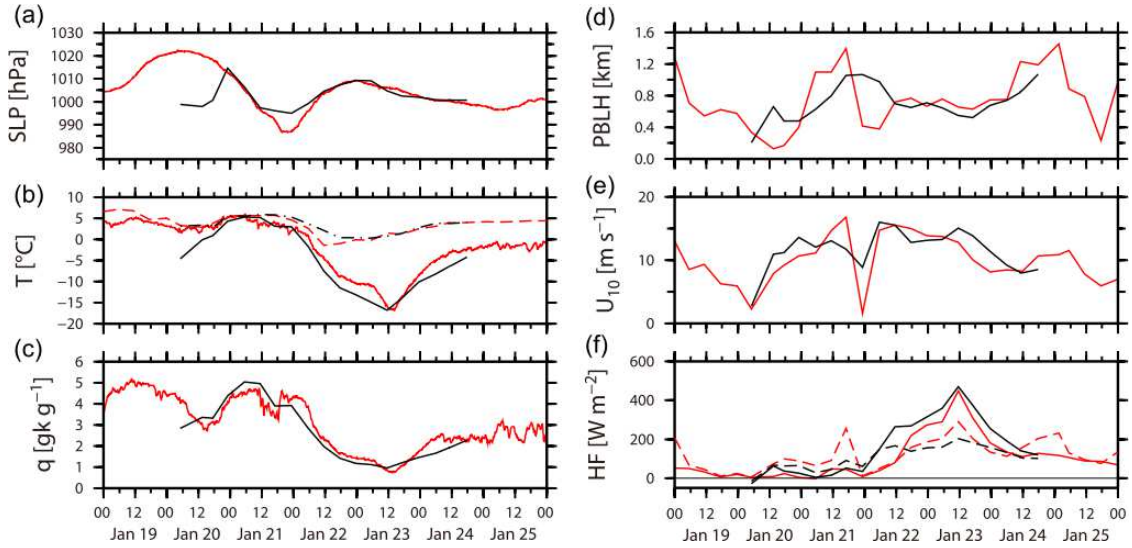

Fig. 2 Comparison of time series of shipboard surface meteorological observations (red) and CNTL (black). (a) SLP, (b) SAT (solid), shipboard measured SST (dot-dashed), and OISST (dashed), (c) surface specific humidity, (d) PBLH, (e) U_{10}, and (f) SHF (solid) and LHF (dashed) along the ship transect (black lines and circles in Fig. 1).

2.3 Numerical experiments

A series of numerical experiments were conducted to examine the roles of surface fluxes in the development and maintenance of a cyclone. A full-physics control model simulation (CNTL) was conducted to reproduce the life cycle of the observed cyclone. The time integration of CNTL started at 21/00:00 and ended at 25/00:00. The relative importance of various physical processes changes during the life cycle of the cyclone and the removal of a certain physical process changes the environment in which the cyclone develops (Føre et al., 2012). Shutting off the physical processes from the development phase makes the interpretation of the results during the mature phase difficult. Thus, two groups of sensitivity experiments with different periods of time integration were designed, following Føre et al. (2012). Time integration in one group of experiments including, no turbulent heat flux (NoTF), no sensible heat flux (NoSF), and no evaporation (NoEV) experiments started at 21/00:00 and ended at 22/00:00, focusing on a development phase of the cyclone. Another group denoted by the capital letter D (delayed) at the end of the abbreviation (NoTF-D, NoSF-D, NoEV-D) focused on the mature phase and began at 22/00:00 and ended at 25/00:00. The initial conditions of these delayed experiments were taken as the output of CNTL at 22/00:00 using the restart functionality of the WRF model. Both surface sensible heat flux and evaporation were turned off in NoTF and NoTF-D. In NoSF and NoSF-D, only the surface sensible heat flux was shut off. In NoEV and NoEV-D, only the surface evaporation was switched off. To compare the relative importance of the surface fluxes with condensational heating, we conducted additional sensitivity experiments (NoMC and NoMC-D), in which both the cloud microphysics and cumulus schemes were shut off.

3. Results

3.1 Model validation

Figure 2 compares surface meteorological observations with model outputs of CNTL. Although the model underestimated the observed SLP minima at around 20/12:00 and 22/00:00, it reproduced temporal variations of SLP correctly. Model output was also in agreement with observations for the SAT, surface specific humidity, planetary boundary layer height (PBLH), wind speed at a height of 10 m (U_{10}), sensible heat flux (SHF), and latent heat flux (LHF).

Model results were further compared with in situ atmospheric soundings (Fig. 3). From 20/00:00 to 21/18:00, in situ atmospheric soundings recorded large RH values from the lower to upper troposphere, suggesting horizontal moisture transport. The tropopause then started to fall from 21/12:00, indicating cyclone development. The wind became strong and veered from southwesterly to northwesterly from 21/12:00 to 22/12:00. This indicated the passage of the cyclone near the ship and was consistent with the tracks of the cyclone (Fig. 1). After 22/00:00, the lower troposphere became more humid (RH exceeding 80%), while dry air dominated (RH below 10%) above approximately the 300-hPa level and there was accompanying tropopause folding. These observed features were successfully reproduced in CNTL, giving us confidence for further analysis as described below.

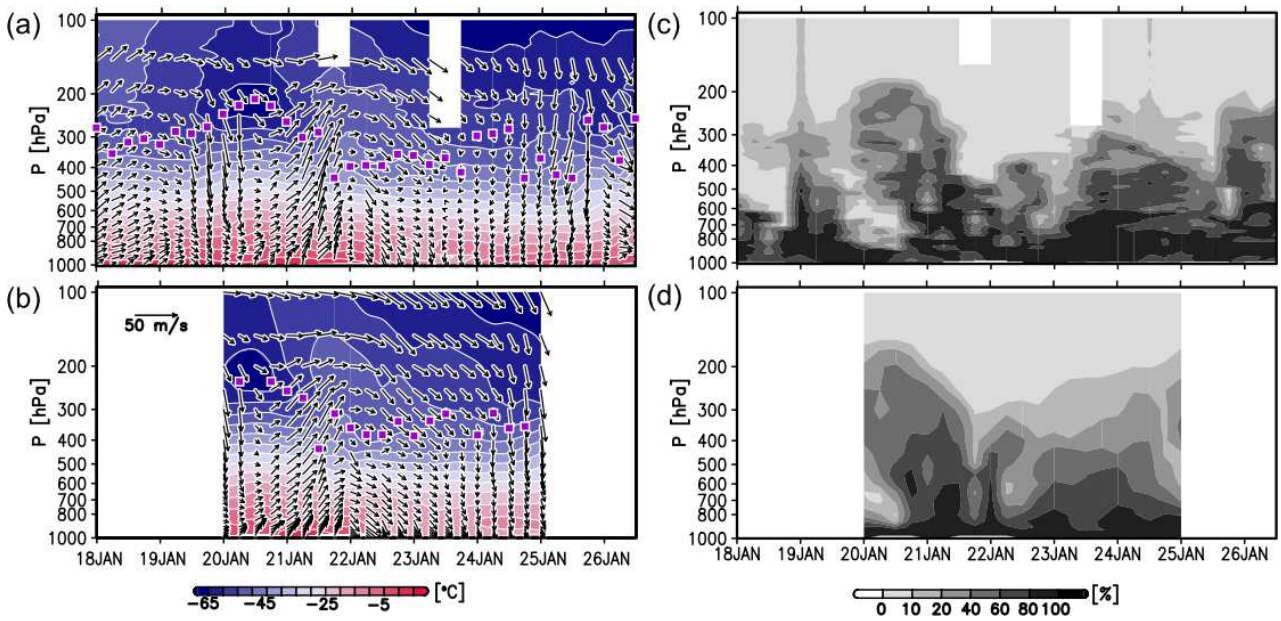

Fig. 3 Pressure–time plots of (a) observed and (b) modelled air temperature and horizontal wind vectors, and (c) observed and (d) modelled RH along the ship transect shown in Fig. 1. Purple squares represent the pressure levels of the tropopause.

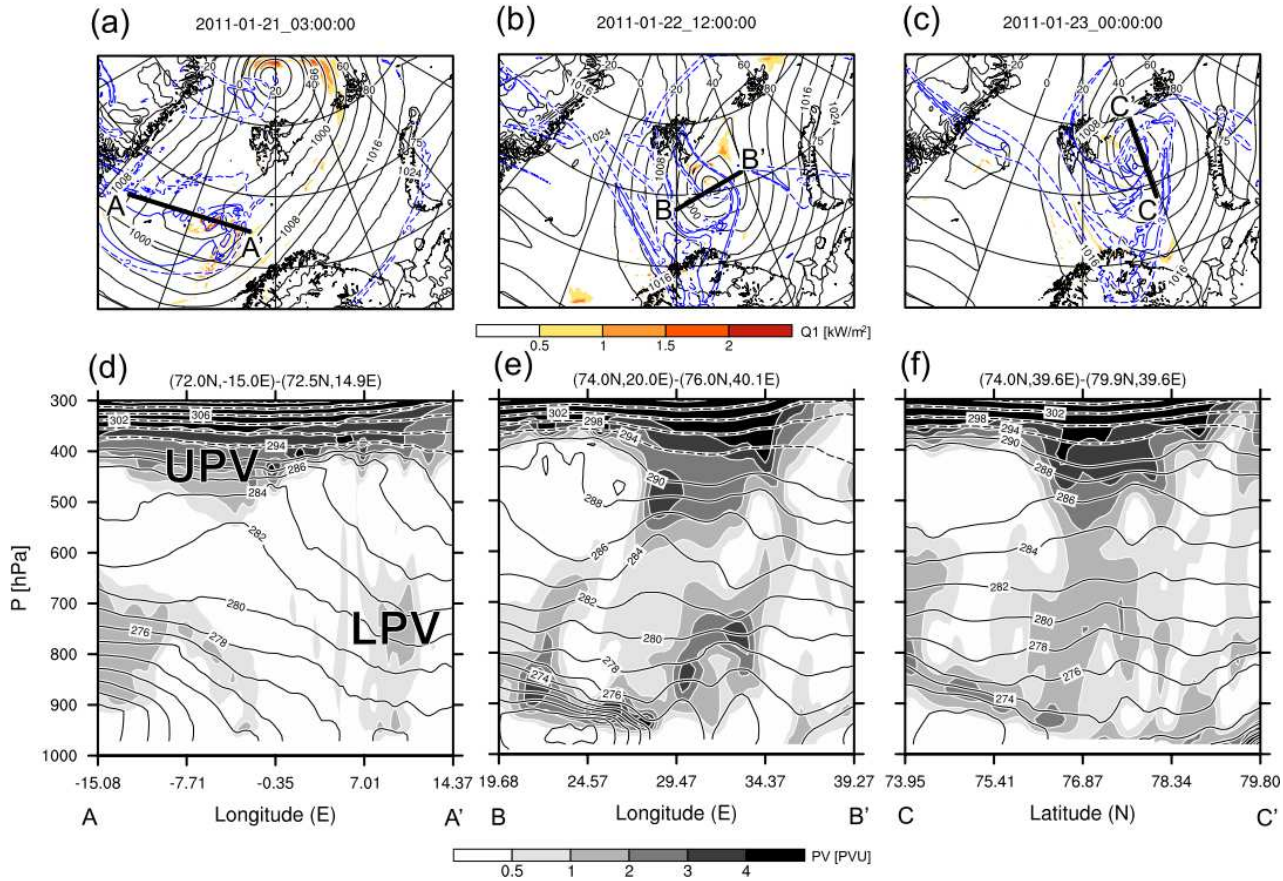

Fig. 4 (Black) Maps of SLP in hPa, (blue) PV at the 300-hPa level in PVU, and (color) vertically integrated condensational heating rate in kWm^{-2} at (a) 21/03:00, (b) 22/12:00, and (c) 23/00:00. Cross sections of (shade) PV and (contour) virtual potential temperature (VPT) along the lines (d) AA´, (e) BB´, and (f) CC´. The contour intervals of the VPT are 2 and 4 K, respectively represented by solid and dashed lines.

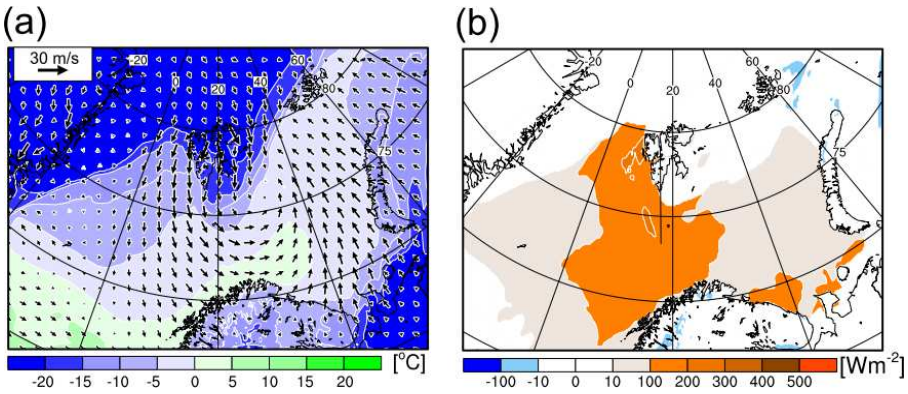

Fig. 5 (a) Maps of (color) SAT and (vector) U_{10} and (b) LHF averaged from 22/00:00 to 23/00:00.

3.2 Life cycle of the cyclone

The cyclone in CNTL initiated north of Iceland and moved towards the east of Svalbard at approximately 21/03:00 (Fig. 4). The cyclone track in CNTL is consistent with that in ERA-Interim data (Fig. 1). The simulated SLP in CNTL was a minimum around 22/00:00 and gradually increased until 24/12:00 (data not shown). The cyclone lasted for more than three days. These features are consistent with satellite infrared images and ERA-Interim data (not shown). During the development phase, air with high values of potential vorticity (PV) exceeding 3 potential vorticity units (PVU; 10^{-6} K m^2 kg^{-1} s^{-1}) at the 300-hPa level extended from Greenland and was located above the surface trough (Fig. 4a, b, d, and e). The vertically integrated condensational heating rate was high east of the surface trough (around the area west of A´ in Fig. 4a). A cross section along the line AA´ shows an upper-tropospheric high-PV anomaly (PV > 1) centered around 4°W and the 400-hPa level (indicated by UPV) while a lower-tropospheric high-PV anomaly (indicated by LPV) dominated east of the upper PV anomaly (Figure 4d). These features (i.e., upper and lower PV anomalies and diabatic heating east of the upper PV anomaly) are consistent with the conditions of Type-C cyclone development proposed by Deveson et al. (2002).

After the development phase, the cyclone moved east of Svalbard and started to decay (Fig. 4c). At the beginning of the mature phase, upper and lower PV anomalies were coupled (Fig. 4f). The cyclone decayed as the upper PV anomaly moved south of the surface cyclone and gradually decoupled with the lower PV anomaly during its mature phase. All the features of the simulated cyclone are consistent with those in the ERA-Interim data (data not shown).

During its mature phase, the cyclone stayed around the ice edge east of Svalbard (Figs. 1 and 4). During this phase, an outbreak of cold air induced by a northerly west of Svalbard due to the cyclone enhanced

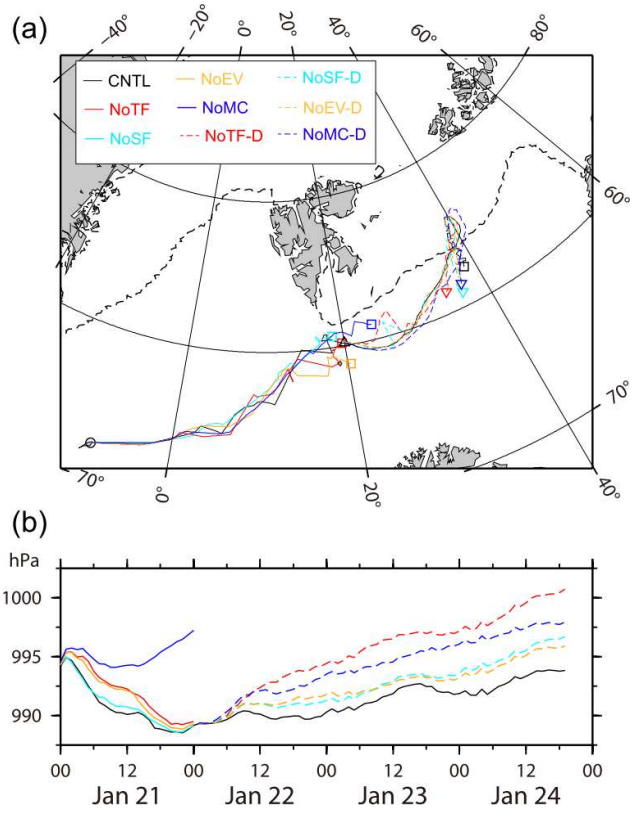

Fig. 6 (a) Tracks of the simulated cyclone and (b) time series of SLP at the storm center. The thick dashed line in (a) indicates the sea-ice edge. Circles in (a) represent the locations of the storm center at 21/00:00. Black and colored squares respectively indicate the locations of the storm center at 25/00:00 and 22/00:00 in CNTL and other experiments (NoTF, NoSF, NoEV, and NoMC). The triangle and inverted triangles respectively indicate the locations of the storm center at 22/00:00 and 24/18:00 in CNTL and the other delayed experiments (NoTF-D, NoSF-D, NoEV-D, and NoMC-D).

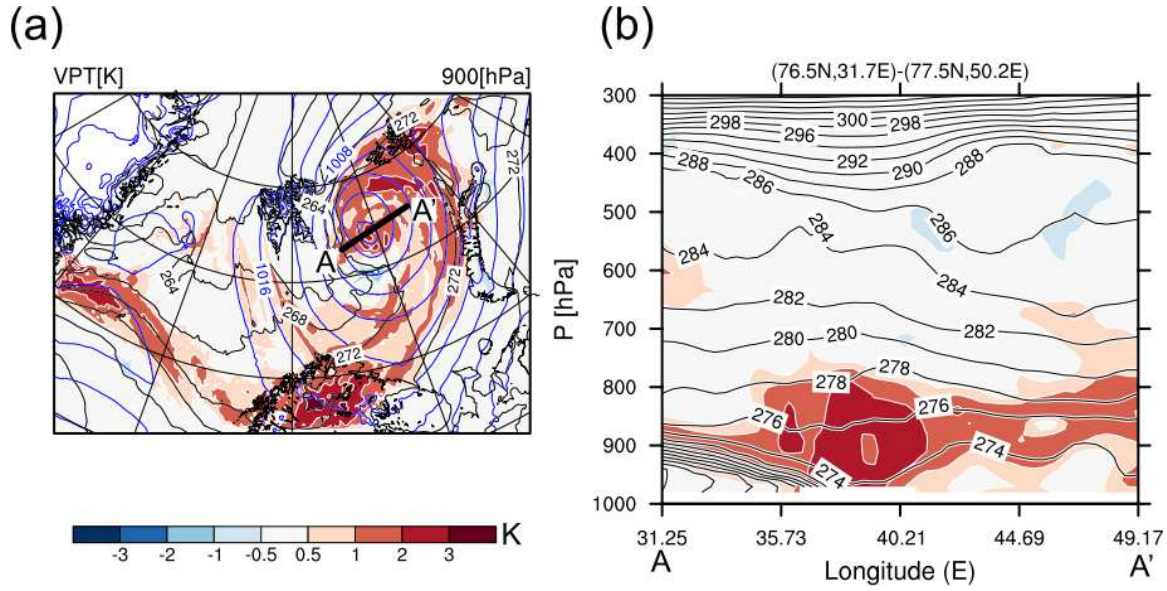

Fig. 7 (a) Map at the 900-hPa level and (b) cross section of differences in VPT between CNTL and NoEV-D in K (color). Black and blue contours represent the VPT in K and SLP in hPa. The thick line AA´ in (a) indicates the location of the cross section in (b).

the surface evaporation (Fig. 5), which may have affected the lifecycle of the cyclone and thermodynamic structure around the cyclone. It is well known that evaporation plays a fundamental role in the life cycle of the tropical cyclone (e.g., Emanuel 2003). However, the development process of the polar cyclone described here is fundamentally different from that of tropical cyclones. The role of evaporation in the life cycle of this cyclone should be different from that in the tropical cyclone and will thus be examined later.

3.3 Sensitivity experiments

Figure 6 shows the track of the cyclone in each sensitivity experiment and time series of the simulated SLP at the storm center. There were no large differences between the tracks of the cyclone in the sensitivity experiments and CNTL. The cyclone hardly deepened when the cloud microphysics and cumulus schemes were switched off during the development phase (NoMC). The SLP at 22/00:00 in NoTF, NoSF, and NoEV was comparable to that in CNTL. In contrast, all the delayed experiments were highly sensitive to the physical processes that were turned off. Condensational heating (NoMC-D) affected the mature phase of the cyclone. NoTF-D saw the strongest effect of the SLP while the effect of turbulent heat flux (NoTF-D) was stronger than that of condensational heating (NoMC-D), which is consistent with the results of Kolstad et al. (2016). The effect of the surface evaporation (NoEV-D) was comparable to that of the surface sensible heat flux (NoSF-D). The effect of the surface evaporation during the mature phase of a cyclone has not been fully addressed in previous studies, and we therefore further examine the results of NoEV-D.

Figure 7 depicts the difference in the virtual potential temperature (VPT) between CNTL and NoEV-D at 23/00:00. CNTL had higher VPT in the lower troposphere around the cyclone than did NoEV-D. Terms in the thermodynamic equation were analyzed to elucidate the dominant processes of this change in VPT.

Figure 8 shows the cross-sections of differences in terms in the thermodynamic equation of the model between CNTL and NoEV-D along the line AA´ in Figure 7a, averaged from 22/01:00 to 23/00:00. The rate of time change in the lower troposphere was positive except in some small areas (Fig. 8a). Local condensational processes dominated the heating in the lower troposphere. Advection also contributed to heating, except near the surface, which is consistent with the results of Screen et al. (2012).

The cloud fraction averaged from 22/01:00 to 23/00:00 (Fig. 9a) indicates the dominance of low-level clouds near the cyclone center. There were also mid-level clouds west of the cyclone center, but changes in cloud fraction were mainly found in the lower troposphere (Fig. 9b), providing evidence for the dominance of condensational heating. In addition, the planetary boundary layer scheme played a role near the surface (Fig. 8e). Longwave radiation counteracted heating except around the 800-hPa level (Fig. 8d). The residual term, relating to physical processes such as horizontal diffusion and shortwave radiation, was negligible (data not shown). The dominance of advection suggests the importance of the remote influence, by which warmer air resulting from diabatic heating is transported from remote areas. The difference

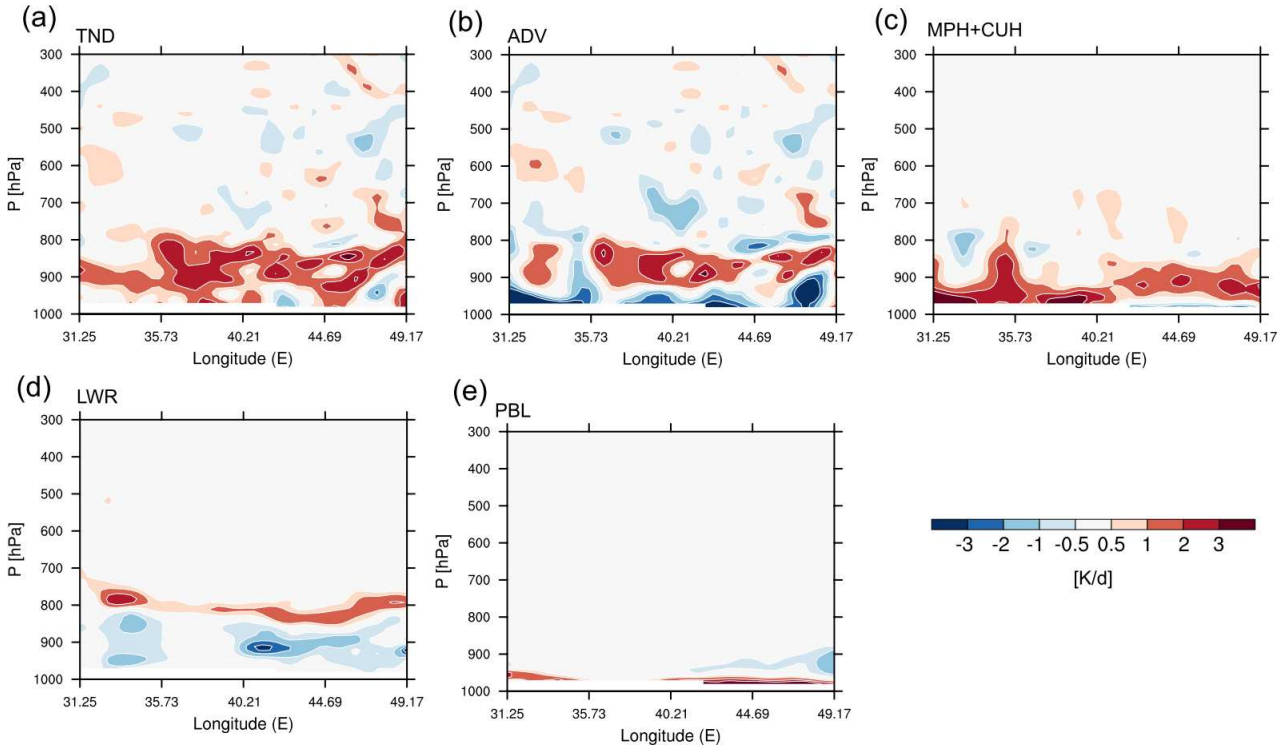

Fig. 8 Cross sections showing differences of terms in the heat budget equation between NoEV-D and CNTL along the line AA´ in Fig. 7a, averaged from 22/01:00 to 23/00:00. (a) Tendency (rate of time change), (b) advection, (c) sum of diabatic heating terms relating to cloud microphysics and cumulus schemes, (d) long-wave radiation, and (e) planetary boundary layer scheme.

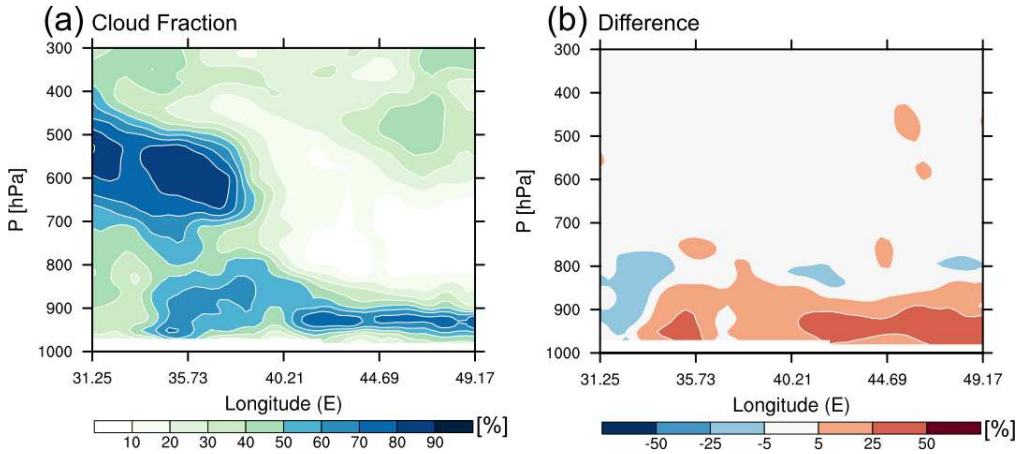

Fig. 9 Cross sections of the cloud fraction in percent: (a) CNTL and (b) difference between NoEV-D and CNTL along the line AA´ in Fig. 7, averaged from 22/01:00 to 23/00:00.

in VPT in Fig. 7(a) suggests the warmer air was created in remote areas around the cyclone and moved into the cyclone center. Trajectory analyses indicate that the VPT of air parcels from around the cyclone near the surface increased, providing evidence of the remote influence (data not shown).

4. Summary and Discussion

The role of surface evaporation in the life cycle of the cyclone and ocean–atmosphere heat exchange in the Barents Sea was investigated through a series of numerical simulations and validated carefully using shipboard surface meteorological observations and atmospheric soundings. An outbreak of cold air and strong winds induced by the cyclone enhanced the surface evaporation during the mature phase of the cyclone. The enhanced evaporation contributed to the longevity of the cyclone. The effect of the surface evaporation was comparable to that of the surface sensible heat flux. An increase in moisture due to surface evaporation caused atmospheric warming in the

lower troposphere over the Barents Sea, as suggested by Inoue and Hori (2011). A detailed thermodynamic analysis revealed that this warming was mainly due to local condensational and boundary layer heating and the advection of warm air.

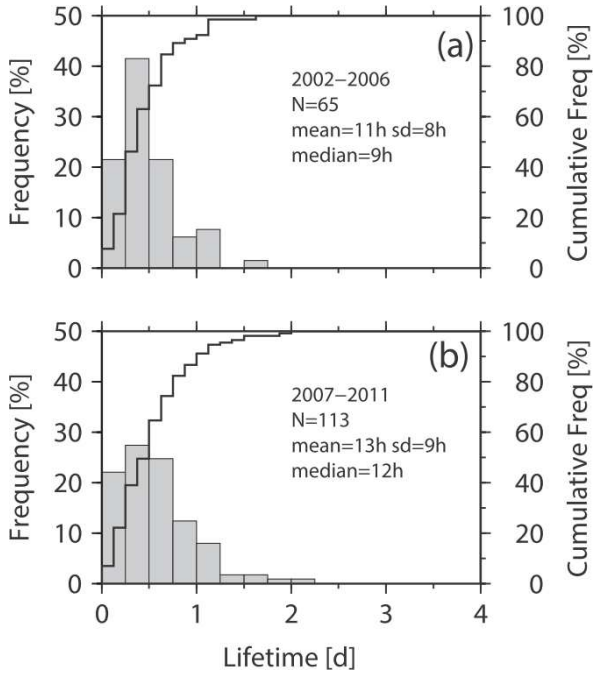

Fig. 10 Histograms of lifetimes of Arctic polar mesocyclones catalogued in the STARS database for (a) 2002–2006 and (b) 2007–2011. Bars and solid lines respectively represent the frequency and cumulative frequency.

Stronger surface winds around the cyclone during the prolonged mature phase should affect the sea-ice distribution. In the sea ice diminishing Arctic, rough seas will contribute to surface evaporation and further contribute to atmospheric warming as shown in this study. Moreover, SST distributions have a rich structure in the Nordic Seas as shown in Fig. 1. The ocean currents should impact such SST distributions and hence the surface evaporation. An interaction between the cyclones and the sea ice distribution and the effect of the sea-ice decline need further investigation because the recent decline in sea ice in the Barents Sea potentially enhances such a warming process.

Although previous studies have paid little attention to the lifetimes of cyclones in the Arctic Ocean (Smirnova et al., 2015), such investigation will be important in the assessment of the effect of cyclones on atmospheric warming in the Arctic. Figure 10 shows histograms of lifetimes of Arctic polar mesocyclones (so-called polar lows) catalogued in the database of Sea Surface Temperature and Altimeter Synergy for Improved Forecasting of Polar Lows (STARS; Eastwood et al., 2012), suggesting an increasing trend in lifetimes. This database does not include cyclones that do not satisfy the definition of a polar low. However, it is worthwhile to expand the lifetime analysis to Arctic cyclones other than polar lows. A long-term trend of the lifetime of cyclones is beyond the scope of this study but should be examined in future research. Continuous monitoring of cyclones is thus an important task. Such monitoring is necessary for the assessment of the long-term change in cyclone characteristics and background environmental parameters (e.g., SST) induced by multidecadal variabilities (Tokinaga et al., 2017) and will contribute to our understanding of the effect of cyclones on Arctic weather and climate. Satellite consternations have been indispensable to study such long-term changes and will continue to be essential for researches in the Arctic climate.

Acknowledgements

The authors thank R. Ingvaldsen and the crews of R/V Johan Hjort of the Institute of Marine Research, Norway, and participants in the field campaign for their help with data collection. The authors also thank K. Hines and the Polar Meteorology Group, Byrd Polar and Climate Research Center, Ohio State University for providing Polar WRF. Constructive comments from two anonymous reviewers and fruitful discussion with W. Yanase, U. Shimada, and S. Watanabe are greatly appreciated. This manuscript was edited by Glenn Pennycook from Edanz Group. This work was supported in part by the Arctic Challenge for Sustainability and the Japan Society for Promotion for Science through Grants-in-Aid for Scientific Research (16H01844, 16H04046, 17H02958, 18H03745, 18KK0292, and 19H05697).

References

Adakudlu, M. and I. Barstad (2011): Impacts of the ice-cover and sea-surface temperature on a polar low over the Nordic seas: a numerical case study. *Q.J.R. Meteorol. Soc.*, **137**: 1716-1730.

Boisvert L.N., D.L. Wu and C.L. Shie (2015): Increasing evaporation amounts seen in the Arctic between 2003 and 2013 from AIRS data. *J. Geophys. Res.*, **120**: 6865–6881.

Boisvert, L.N., A.A. Petty and J.C. Stroeve (2016): The impact of the extreme winter 2015/16 Arctic cyclone on the Barents -Kara Seas. *Mon. Wea. Rev.*, **144**: 4279 – 4287.

Dai, A., D. Luo and 2 others (2019): Arctic amplification is caused by sea-ice loss under increasing CO_2. *Nat. Comm.*, **10**: 121, https://doi.org/10.1038/s41467-018-07954-9.

Dee, D.P., S.M. Uppala and 34 others (2011): The ERA-Interim reanalysis: configuration and performance of the data assimilation system. *Q.J.R. Meteorol. Soc.*, **137**: 553–597.

Deser, C., R. Tomas, M. Alexander and D. Lawrence (2010): The seasonal atmospheric response to projected Arctic sea ice loss in the late twenty-first century. *J. Clim.*, **23**: 333–351.

Deveson, A.C., K.A. Browning and T.D. Hewson (2002): A classification of FASTEX cyclones using a height-attributable quasi-geostrophic vertical-motion diagnostic. *Q.J.R. Meteorol.*

Soc., **128**: 93-117.
Dudhia, J. (1989): Numerical study of convection observed during the Winter Monsoon Experiment using a mesoscale two-dimensional model. *J*. *Atmos*. *Sci*., **46**: 3077–3107.
Dufour, A., O. Zolina and S. K. Gulev (2016): Atmospheric moisture transport to the Arctic: Assessment of reanalyses and analysis of transport components. *J*. *Clim.*, **29**: 5061-5081.
Eastwood, S., Y. Gusdal and 4 others (2012): *STARS-DAT v3 user manual version 3.1*. Norwegian Meteorological Institute, Oslo, Norway, 40 pp.
Emanuel, K. (2003): Tropical Cyclones. *Annual Review of Earth and Planetary Sciences*, **31**: 75-104.
Føre, I., J.E. Kristjánsson and 4 others (2012): A 'hurricane-like' polar low fuelled by sensible heat flux: high-resolution numerical simulations. *Q*.*J*.*R*. *Meteorol*. *Soc*., **138**: 1308–1324.
Hao, M., Y. Luo, Y. Lin, Z. Zhao and 2 others (2019): Contribution of atmospheric moisture transport to winter Arctic warming. *Int*. *J*. *Climatol*., **39**: 2697– 2710.
Hines, K.M. and D.H. Bromwich (2008): Development and testing of polar weather research and forecasting (WRF) model. Part I: Greenland ice sheet meteorology. *Mon*. *Wea*. *Rev*., **136**: 1971-1989.
Hong, S.Y., Y. Noh and J. Dudhia (2006): A new vertical diffusion package with an explicit treatment of entrainment processes. *Mon*. *Wea*. *Rev*., **134**: 2318–2341.
Inoue, J. and M.E. Hori (2011): Arctic cyclogenesis at the marginal ice zone: A contributory mechanism for the temperature amplification? *Geophys*. *Res*. *Lett*., **38**: L12502, https://doi.org/10.1029/2011GL047696.
Kain, J.S. (2004): The Kain-Fritsch convective parameterization: an update. *J*. *Appl*. *Meteor*., **43**: 170–181.
Kolstad, E.W., T.J. Bracegirdle and M. Zahn (2016): Re-examining the roles of surface heat flux and latent heat release in a "hurricane-like" polar low over the Barents Sea. *J*. *Geophys*. *Res*., **121**: 7853‐ 7867.
Mlawer, E.J., S.J. Taubman and 3 others (1997): Radiative transfer for inhomogeneous atmospheres: RRTM, a validated correlated-k model for the longwave. *J*. *Geophys*. *Res*., **102**: 16663-16682.
Moore, G.W.K. (2016): The December 2015 North Pole warming event and the increasing occurrence of such events. *Sci*. *Rep*., **6**: 1-11.
Morrison, H., G. Thompson and V. Tatarskii (2009): Impact of cloud microphysics on the development of trailing stratiform precipitation in a simulated squall line: comparison of one- and two-moment schemes. *Mon*. *Wea*. *Rev*., **137**: 991-1007.
Nakanishi, M. and H. Niino (2009): Development of an improved turbulence closure model for the atmospheric boundary layer. *J*. *Meteorol*. *Soc*. *Jpn*., **87**: 895-912.
Reynolds, R.W., T.M. Smith and 4 others (2007): Daily high-resolution-blended analyses for sea surface temperature. *J*. *Clim*., **20**: 5473–5496.
Screen, J.A. and I. Simmonds (2010): The central role of diminishing sea ice in recent Arctic temperature amplification. *Nature*, **464**: 1334–1337.
Screen, J.A., C. Deser and I. Simmonds (2012): Local and remote controls on observed Arctic warming, *Geophys*. *Res*. *Lett*., **39**: L10709, doi:10.1029/2012GL051598.
Serreze, M.C. (1995): Climatological aspects of cyclone development and decay in the Arctic, *Atmosphere-Ocean*, **33**: 1-23, https://doi.org/10.1080/07055900.1995.9649522.
Skamarock, W.C., J.B. Klemp and 7 others (2008): A description of the Advanced Research WRF Version 3. *NCAR technical note NCAR/TN-475+STR*, NCAR: Boulder, Colorado, USA, 113pp., doi: 10.5065/D68S4MVH.
Smirnova, J.E., P.A. Golubkin and 3 others (2015): Polar low climatology over the Nordic and Barents seas based on satellite passive microwave data. *Geophys*. *Res*. *Lett*., **42**: 5603-5609.
Tokinaga, H., S.P. Xie and H. Mukougawa (2017): Early 20th-century Arctic warming intensified by Pacific and Atlantic multidecadal variability, *Proc*. *Nat*. *Acad*. *Sci*. **114**, 6227-6232.
Zahn, M., M. Akperov and 3 others (2018) Trends of cyclone characteristics in the Arctic and their patterns from different reanalysis data. *J*. *Geophys*. *Res*., **123**: 2737-2751.

Summary in Japanese

和文要約

低気圧を媒介とした北極海における海洋ー大気間の熱交換のメカニズム： 2011 年 1 月にバレンツ海で観測された低気圧の事例解析

万田敦昌 [1], 三井拓 [2], 猪上淳 [2, 3], 堀正岳 [3, 4], 河本和明 [5], 小松謙介 [1]

[1] 三重大学, [2] 総合研究大学院大学, [3] 国立極地研究所, [4] 海洋研究開発機構, [5] 長崎大学

北極温暖化における低気圧の果たす役割の重要性が近年の研究で指摘されている。既往の多くの研究は中緯度からの顕熱・潜熱の水平輸送に焦点を当てており，北極海の蒸発の影響に着目したものは無い。そこで 2011 年 1 月にバレンツ海で行われた現地観測で捉えられた低気圧を対象として，海面からの蒸発が低気圧に及ぼす影響を数値シミュレーションによって調べた。海面からの蒸発は，低気圧の長寿命化に寄与し，その効果は顕熱と同程度であった。熱収支解析から海面からの蒸発は凝結加熱，境界層における加熱，および暖気移流の強化を通じて，気温を上昇させていることが明らかとなった。近年の海氷減少とそれに伴う蒸発の強化は，本研究で示された低気圧を媒介とした海洋ー大気間の熱交換を促進し，北極海のさらなる温暖化に寄与している可能性がある。

Okhotsk Sea and Polar Oceans Research 4 (2020) 10-17

Article

Calculation of penetration distance during ship ramming in multi-year ice

Junji SAWAMURA[1], Hajime YAMAGUCHI[2], Shuki USHIO[3], Yutaka YAMAUCHI[4]

[1] *Graduate School of Engineering, Osaka University, Osaka, Japan*
[2] *Graduate School of Frontier Sciences, The University of Tokyo, Kashiwa, Japan*
[3] *Meteorology and Glaciology Group, National Institute of Polar Research, Tachikawa, Japan*
[4] *Technical Research Center, Japan Marine United Corporation, Tsu, Japan*

(Received September 23, 2019; Revised manuscript accepted November 25, 2019)

Abstract

The Japanese Antarctic research icebreaker *Shirase* has encountered severe ice conditions during her operations in the Antarctic sea ice. Ramming performance influences the voyage schedule and safe operation in heavy ice conditions. This paper presents a proposed method of calculating the penetration distance during ramming operations. Ship–ice collision, ship slide–up, and ice failure were modeled. Bending failure was applied to ramming icebreaking criteria. The penetration distance obtained using the proposed method was compared with those from ship trials in the Antarctic sea ice.

Key words: Antarctic sea ice, energy conservation, icebreaking, multi-year ice, ramming

1. Introduction

The Japanese Antarctic Research Expedition (JARE) was begun in 1956. The Antarctic research icebreaker *Shirase* II has transferred cargoes and scientists to the Japanese Antarctic research station (Syowa station) since 2009. *Syowa* station is located in Lützow–Holm Bay, which is often covered with the multi-year ice (Sawamura, 2016). *Shirase* is therefore often required to ram the multi-year ice. Ramming icebreaking requires more operation time and fuel than continuous icebreaking. Therefore, ramming performance strongly affects Antarctic voyage schedules and safe operations (Yamauchi and others, 2009).

During ship ramming, the icebreaker repeats backward and forward motion and breaks the sea ice by ship–ice impact and slide–up of the ship onto the ice. To model ship ram events, the complicated ship–ice interactions during ramming must be described. Earlier studies related to calculation of ship ramming were conducted by Popov and others (1967) and Vaughan (1986). They have been cited by Dalay and Riska (1990). The calculations have assumed the ship–ice interactions during ship ramming to be the ship–ice impact problem. They have derived a simple formula of ramming force, in which energy conservation in modeling of ship ram is applied. Blanchet and others (1990) have applied the energy conservation principle to represent the ship–ice impact and ship slide-up with and without the flexural response of ship during ship ramming. They calculated the kinematic energy of ship–ice interactions. Kishi and others (1997) used the energy balance model to predict the penetration distance of ship ramming based on measured and model test data. Ringsberg and others (2014) analyzed the relation between measured ship motions and ice loads. They proposed the computational model to identify ramming force during ship–ice events in the heavy ice conditions. Takahashi and others (2019) investigated measured data of impact velocity, penetration distance, and turning angle of the icebreaker *Shirase*. They predicted the required time for turning operations of ship ramming. Use of the present predictions of ship ramming remains limited because most predictions require measured or model test data of ship ramming.

This paper presents calculation of the penetration distance of ship ramming based on energy conservation in ship–ice interactions of ship ramming. The phenomena of ship–ice impact, ship slide–up, and ship–ice friction are involved in the energy balance during ship ramming. Bending failure of plate ice is applied to the ship ramming icebreaking. The proposed method calculates the penetration distance. Results were compared with the penetration distance of icebreaker *Shirase* measured in the 55th Japanese Antarctic Research Expedition (JARE 55) on 2013 and 2014.

2. Ship ramming in the Antarctic sea ice

Shirase conducted her operations in the Antarctic sea ice for the 55th Japanese Antarctic Research Expedition (JARE 55) during December 2013 through March 2014. During the outbound voyage to *Showa* station, *Shirase* started her ramming operations from December 18, 2013, when she entered the multi-year ice (69°00’N, 39°05’E), and continued until January 4, 2014 when she berthed at *Showa* station (69°00’N, 39°38’E). The ramming in multi-year ice was done 1952 times. *Shirase* is equipped with a ship-monitoring system that records ship motion data during her voyage (Yamauch and others, 2011). This paper used ship data related to the ramming, such as ship

speed, GPS location, ship power, ice thickness, etc.

2.1 Ice thickness

The ice thickness was measured by an electro–magnetic induction sensor (EM sensor) installed at the starboard shoulder. Visual observation and image analysis were also used for ice thickness measurements. Image analysis measures the ice thickness using the digital camera and laser measure. The digital camera captures the vertical cross section of ice when the ship breaks the ice and the ice is rotated by the ship advancing. At the same time, the laser measures the distance between the digital camera and the ice. The length of the 1 pixel's image is obtainable by the function with the distance from the digital camera to the ice. The ice thickness is calculated by the number of the pixels in the ice cross section and the length of the 1 pixel's image. (Sawamura, 2016). EM sensor can measure only the total sea ice thickness (snow+ice). Others can measure snow and ice thickness separately. The time interval of the EM sensor is 1 s, and others sensor frequencies are 3 hours. Image analyses during water flushing performance tests were conducted in each ramming. The time interval was varied from 5 to 10 min depending on each ramming operation. In the water flushing system, water pumps with nozzles at the bow flush the ice to reduce the friction between hull and ice. Water flushing was used on and off alternately during water flushing performance tests. Tests were conducted during 18:50 (UTC) on Jan. 3, 2014 and 3:07 (UTC) on Jan. 4, 2014.

Table 1 shows the average ice and snow thickness at for 2013/12/22–23 (Area 01), 2014/01/03–04 (Area 02) and the water flushing test (Area 03). The total sea ice thickness obtained using the three method show moderately good agreement. The tendency of the total thickness is that visual observations revealed the greatest thickness, the EM sensor obtained an intermediate result, and image analysis obtained minimal thickness. The average sea ice thickness on Feb. 22 and 23 in 2013 (Area 01) were about 5 m. The average thickness on Jan. 3, 2014 (Area 02) was about 4 m. The average thickness on Jan. 4, 2014 (Area 02) was about 3 m. In the water flushing test (Area 03), the differences of ice thickness among the three methods become larger than those in other areas (Area 01 and Area 02). The measured thickness during the water flushing test became approximately 2.5–3.5 m. The snow thickness during Feb. 22 and 23 in 2013 (Area 01) was greater than 1 m; during Jan. 3 and 4, 2014 (Area 02 and Area 03), it was less than 0.5 m. The measured data shows that the sea ice thickness gradually diminished as the days passed, which means the sea ice conditions in the early period of ramming operations were extremely heavy. Those in the end period close to Showa station were moderate.

Table 1. Measured ice and snow thickness Unit [m]

		2013/12 (Area 01)		2014/01 (Area 02)		Flush (Area
		22	23	03	04	03)
EM sensor	Ice + snow	5.18	5.13	3.53	2.65	3.42
Visual observation	Ice	3.90	4.00	4.25	2.61	2.40
	Snow	1.50	1.42	0.23	0.29	0.23
	Ice + snow	5.40	5.42	4.48	2.90	2.63
Image analysis	Ice	3.98	3.10	3.12	1.96	2.02
	Snow	1.19	1.39	0.42	0.52	0.27
	Ice + snow	5.17	4.49	3.54	2.48	2.29

Table 2. Average value in one day of the maximum ship speed and thrust of each ship ramming

Date	Speed [m/s]	Thrust [kN]
2013/12/22	5.77	2068
2013/12/23	5.78	2338
2014/01/03	5.56	2168
2014/01/04	5.18	2156
Water flushing	5.31	2194

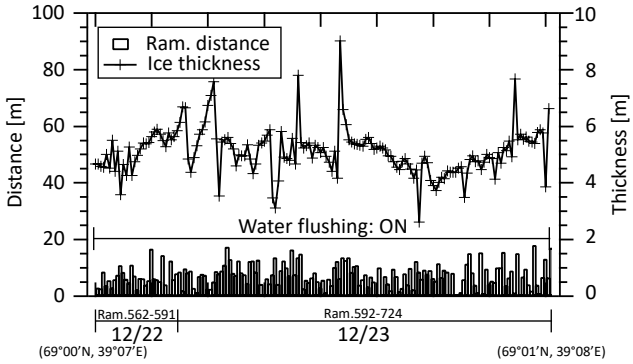

Fig. 1 Measured penetration distance and ice thickness on December 22 and 23, 2013 (Area 01, Ram. No. 562–724)

2.2 Penetration distance

The penetration distance of ramming is defined as the distance between arrival points of the present and preceding ram. The GPS data obtained from the ship-monitoring system were used to calculate the ship location. The GPS data were obtained every 1 s. The ship positions were accurate to around 10 m in GPS and around 7m in MSAS from the catalog data. Water flushing was done from December 18, 2013 to January 1, 2014. Moreover, water flushing was used during water flushing performance tests. Water flushing enables elongation of the ramming distance, especially for the ram with the thick snow. Table 2 shows the average value in one day of the maximum ship speed and thrust. The maximum ship speed and thrust of each ship ramming

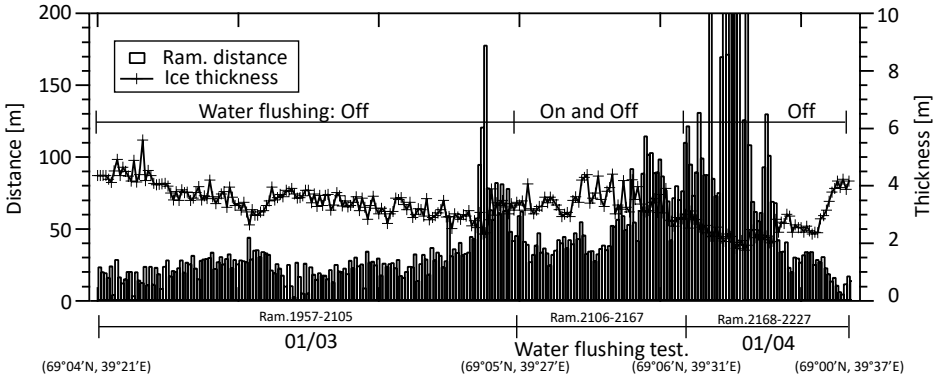

Fig. 2 Measured penetration distance and ice thickness on January 3 and 4, 2014 (Area 02 and Area 03, Ram. No. 1957–2227)

were unchanged during the ramming operations, which reveals the operational conditions were constant during ship ramming operation.

Fig. 1 portrays the measured penetration distance and the total sea ice thickness of each ramming in Area 01. Fig. 2 shows the penetration distance and the total sea ice thickness in Area 02 and Area 03. The total sea ice thickness measured by EM sensor was used in Figs. 1 and 2. In Fig. 1, the average penetration distance of one ramming is 7 m. The total penetration distance in Area 01 is 1187 m. In Fig. 2, the average penetration distance of one ramming is shown as 48 m. The total penetration distance Area 02 and Area 03 is 6978 m. The penetration distance in the heavy ice condition (Area 01) with total thickness greater than 4 m is extremely short; within 20 m. The penetration distance in the light ice condition (Area02 and Area 03), for which the total thickness becomes less than 3 m increases rapidly to longer than 100 m. Moreover, for sea ice thickness of less than 2 m, the penetration distance is greater than 200 m. Results demonstrate that the penetration distance is sensitive to the ice thickness. In Lützow–Holm Bay during December 2013 and January 2014, ice thickness of about 2 m apparently marked the transition from continuous to ramming icebreaking mode. For the short penetration distance within 10 m in the heavy ice conditions (Area 01), the accuracy of the ship positon obtained from GPS must be improved.

3. Method of ship ramming calculation

3.1 Energy conservation model

Vinogradov (Nozawa, 2006) proposed a formula to predict the maximum ice force during ship ramming based on the principle of energy conservation. Vinogradov's approach is as follows;

- The ship strikes the ice, and slides up on the ice using the kinetic energy and propeller thrust energy.
- The ice downward force increases with increase of gravitational force during the ship slide–up on ice.
- The kinetic energy and propeller thrust energy is expended in the ship–ice collision, potential energy and friction during the ship slide–up on ice.
- The ship breaks the ice when the ice downward force exceeds the ice breaking force before all available kinetic energy is expended.

The energy balance during ship ramming is expressed as;

$$(E_0 - E_1) + E_2 = E_3 + E_4 + E_5 \ , \qquad (1)$$

in which the following variables are defined.
E_0 = kinetic energy before ship ram
E_1 = kinetic energy after ramming icebreaking
E_2 = propulsive thrust energy
E_3 = energy dissipation of ship–ice collision
E_4 = potential energy of ship slide–up on ice
E_5 = energy dissipation of ship-ice friction.

E_0 ~E_5 are expressed as shown below.

$$\begin{aligned} E_0 - E_1 &= \frac{W}{2g}({v_0}^2 - {v_1}^2) \\ E_2 &= T \cdot S \\ E_3 &= \frac{W}{2g}({v_0}^2 \sin^2\phi)(1 - e^2) \\ E_4 &= \int_0^{Z_1} P_1 dz + \int_0^{\theta_1} P_1 q d\theta \\ E_5 &= \frac{1}{\sin\phi}\int_0^{Z_1} F dz + \frac{1}{\sin\phi}\int_0^{\theta_1} F q d\theta \end{aligned} \qquad (2)$$

In those equations, v_0 represents the ship velocity before the ship ramming, v_1 denotes the ship velocity after ramming icebreaking, W stands for ship displacement, g is the gravitational constant, T denotes the mean propulsive thrust during ship ramming, S expresses the progress distance into the ice, ϕ signifies the stem angle, and e is the coefficient of restitution of the ship–ice collision. Z_1 represents the reduction of the average draft. Also, θ_1 is the change of trim angle during the ship ramming. P_1 stands for the vertical force at the ship–ice collision surface. F expresses the friction force on the

collision surface. The progress distance S and friction force F are expressed as

$$S = (Z_1 + q\theta_1)\cot\phi, \tag{3}$$
$$F = f_i\left(P_1\frac{\cos\phi}{\cos\beta} + T\frac{\cos\phi}{\cos\beta}\right).$$

Therein, the following variables are used:

$$Z_1 = \frac{P_1}{\rho A_W g}, \tag{4}$$
$$\theta_1 = \frac{P_1 q}{W \cdot KM_L}.$$

In those equations, q denotes the distance between the ship–ice collision point and the center of floatation, β is the cosine of the frame angle, f_i is the coefficient of ship–ice friction, A_W represents the area of waterline, KM_L represents the height of longitudinal metacenter, ρ denotes the seawater density. Also, Eqs. 2–4 are substituted into Eq. 1, with the vertical ice force, P_1, expressed by Eq. (5).

$$P_1 = XT - \left[X^2T^2 + \frac{Y}{A}W^2\frac{{v_0}^2\{1-(1-e^2)\sin^2\phi\}-{v_1}^2}{gd}\right]^{\frac{1}{2}} \tag{5}$$

In that equation, the following variables are used.

$$A = \frac{W}{\rho A_W g d} + \frac{q^2}{KM_L d},$$
$$X = \frac{1-\frac{f_i}{\cos\beta}\tan\phi}{1+\frac{f_i}{\cos\beta}\cot\phi}\cot\phi, \tag{6}$$
$$Y = \frac{1}{1+\frac{f_i}{\cos\beta}\cot\phi}.$$

The ice is broken by ship ramming when P_1 is greater than the ice bearing force P_{ice}.

3.2 Ice breaking

Failure mechanisms by ship ramming are complicated. They include the local and global failure of bending, crushing, splitting, and flaking. Because few data have been collected on the behavior of icebreaking during ship ramming, the mechanism of the failure in ship ram has not been understood precisely. The analysis of this paper relied upon the simple assumption that icebreaking by ship ram occurs by local crushing on the ice edge and the bending failure of the plate ice.

At the points of ship–ice contact, ice crushing at the ice edge takes place as a ship advances in sea ice. The ice force increases concomitantly with increased crushing area of the ice edge. The ice force nominal to the collision surface, F_{nom}, is given as;

$$F_{nom} = A_c\sigma_c, \tag{7}$$

where A_c represents the crushing area on the ship–ice

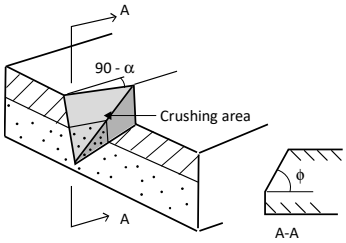

Fig. 3 Assumed stem and crushing area

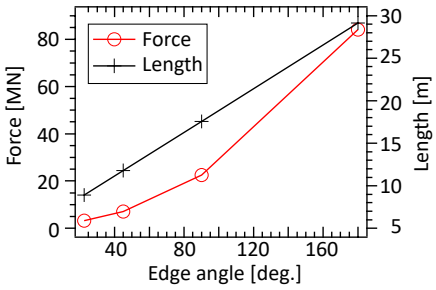

Fig. 4 Icebreaking force and length calculated using FSI (force increasing rate = 10MN/s)

collision surface, σ_c denotes the ice crushing strength, which is called the mean value of crushing pressure by Kujala, 1994, and the average pressure by Daley, 1999. As the crushing area A_c increases, the crushing pressure σ_c decreases (e.g. Frederking, 2003, Frederking and Ritch, 2009). This crushing pressure-area relationship has scale dependency. For large contact area, the mean value of crushing pressure asymptotically approaches to a constant (Kujala, 1994). In this study, constant value of compression strength of ice is used as crushing pressure.

The crushing area, A_c, is calculated based on the collision geometry between the ship and ice. Daley (1999) calculated the nominal crushing area for different collision geometries (e.g. V wedge, symmetric spoon indentation, and right-apex oblique indentation) when he derived the force equation for ship–ice and structure–ice collision problems of ship ram. In this study, the collision between the wedge bow and 180° ice edge (V wedge indentation) was assumed. Reduction of draft Z_1 and change of the trim angle θ_1 were omitted from the calculation of A_c. Figure 3 depicts the crushing area by the geometrical relation between the stem and the ice edge.

The kinematic friction force is presented on the crushing surface. Coulomb type friction is assumed.

$$F_{fric} = f_i F_{nom} \tag{8}$$

The total ice force normal to the collision surface is obtainable by the sum of the collision force F_{nom} and friction force F_{fric}. Ice crushing occurs until the crushing area increases and the downward ice force becomes sufficient to generate ice bending failure.

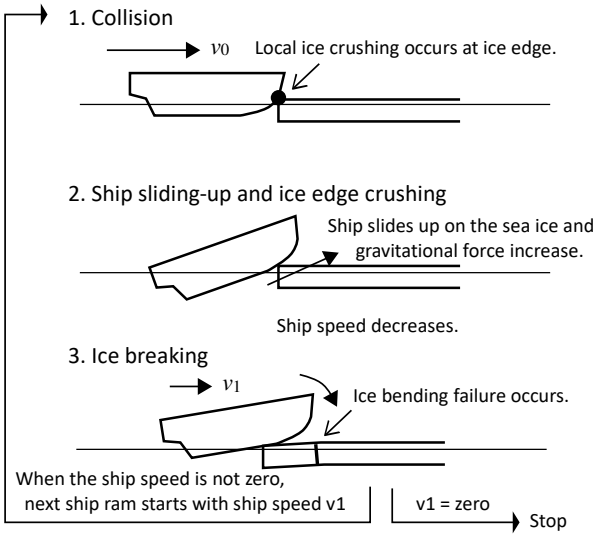

Fig. 5 Ship ramming scenario

Bending failure of the plate ice occurs when the bending stress in the plate ice, σ_b, increases as the ship advances and exceeds the flexural strength of the ice, σ_f. σ_b is calculated using fluid–structure interaction (FSI) in which the dynamic effect of fluid underneath the plate ice is included along with plate ice bending (Sawamura and others, 2008). Ice bending in various ship–ice conditions (e.g. ice edge angle, thickness, and ship speed) is calculated using FSI. A database of the icebreaking force P_{ice} was prepared. In the ship ramming calculations for different ship–ice conditions, the icebreaking force is obtainable from this database (Sawamura and others, 2009). Figure 4 presents an example of database of plate icebreaking by ship ramming.

3.3 Ship ramming

A ship ramming scenario is idealized using the Vinogradov's approach. The ship ramming scenario is portrayed in Fig. 5. The penetration distance is calculated as described below.

- The ship strikes the ice edge with initial velocity v_0.
- The ship slides up on the sea ice. At the same time, the ice edge is broken by ice crushing.
- Ice downward force increases concomitantly with increase of the gravitational force that are created by the ice crushing and ship's slide-up.
- Ice bending failure occurs when the ice downward force P_1 exceeds the ice bearing force P_{ice}. The ship velocity decreases v_1 by the ship's slide-up and ice failure.
- The penetration distance S is calculated by the distance between arrival (ice breaking) points of the present and preceding ram. The total penetration distance S_{total} is calculated as the sum of each penetration distance S.

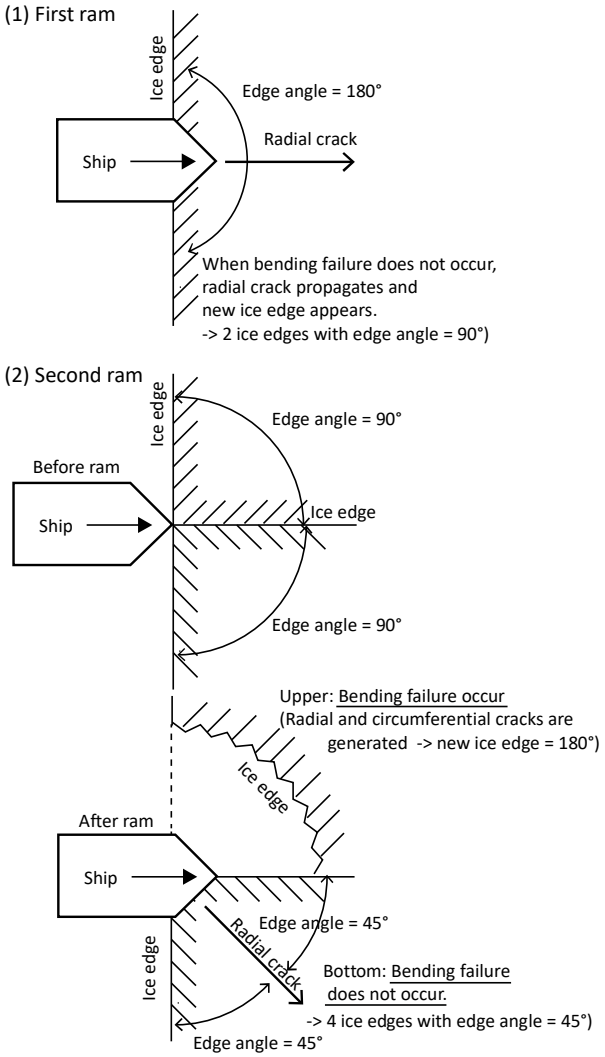

Fig. 6 Idealization of the radial and circumferential cracking of ship ram

The observations of the ship–ice interactions have revealed that ice failure begins by radial cracking starting from the ship–ice collision point, forming a circumferential crack. Ice breaks and falls off the plate ice by the penetration of circumferential crack. The calculations should include the effect of these cracks. In the calculations, when the ice bending failure is not occurred by the preceding ship ramming, only radial crack propagates. The ice edge is divided by the radial crack. The ice plate with two ice edges is generated, in which the edge angle is half size before preceding ship ramming. The ship ram starts for the plate ice with two ice edges. A schematic of ice breaking by radial and circumferential cracks is presented in Fig. 6.

4. Calculation of penetration distance

The measured ship speed, thrust, and the ice thickness were used for ramming distance calculations. The ship speed and thrust were measured respectively every 0.1 s and 1 s. In ship ramming, the ship speed decreases from

the maximum speed to zero as the ship moves through the sea ice. The maximum speed when the ship collides with the ice edge and the mean thrust during the ship ram (from maximum to zero speed) was used as the input data for calculations. The ice thickness measured by the EM sensor at zero speed when the ship ramming has just ended is used.

4.1 Mechanical properties of ice

The mechanical properties of sea ice were not measured in JARE 55. The flexural strength, however, is most important parameter of bending failure of ice. The flexural strength of multi-year ice in JARE 51 (Dec. 2009 – Mar. 2010) was estimated by the empirical formula using the brine volume of sea ice. The flexural strength at two locations in multi-year ice were 0.5 MPa and 0.8 MPa (Yamauch and others, 2011). For coefficient of restitution of sea ice, there is no available measured data. The coefficient of restitution obtained from the collision tests with pure ice block and ice sphere are available (Araoka and other, 1978). The coefficient of restitution of the pure ice was around 0.7.

The sensitive analysis are carried out for ice flexural strength and coefficient of restitution. The ice flexural strength from 0.3 MPa to 1.0 MPa and the coefficient of restitution from 0.0 to 1.0 are selected. Young's modulus, compression strength, and coefficient of friction of ice used in the model test of ship in level ice (Sawamura and others, 2016) are selected, because the flexural strength (0.5 MPa - 0.66 MPa) are similar values of those in JARE 51. The calculations were carried out for Area 01, Area 02, and Area 03. The principal dimensions of the icebreaker *Shirase* and the mechanical properties of the sea ice are presented respectively in Tables 3 and 4.

Table 3. Principal dimensions of icebreaker *Shirase*

Length of waterline	L_{wl}	126 m
Maximum width	B_m	28 m
Draft	d	9.2 m
Displacement		22000 ton
Bow angle		19 deg.

Table 4. Mechanical properties of sea ice

Young's modulus	E	300 MPa
Flexural strength	σ_f	0.5 MPa (0.3 MPa - 1.0 MPa)*
Compression strength	σ_c	0.7 MPa
Coefficient of Friction		0.1
Coefficient of restitution		0.7 (0 - 1)*

*Round brackets; for sensitive calculations

Table 5 and Table 6 show average of the calculated penetration distance using different bending strength (from 0.3 to 1.0 MPa) and coefficient of restitution (from 0.0 to 1.0). When the more than 10 times ramming breaking are continued in one ship's ram, the calculation assumes the icebreaking to be continuous icebreaking instead of ramming icebreaking. From Table 5, and Table 6, ship ramming for icebreaking that was judged to be continuous icebreaking in the calculations was excluded. The average of the calculated penetration distance increase with increases of the flexural strength, but is unchanged by the coefficient of restitution. The average of the measured penetration distance was 22.7 m, which are larger than the calculated ones in Tables 5 and 6. Therefore, for the comparison of penetration distance (following subsection), the calculated results using the flexural strength of 0.5 MPa (the smaller one measured in JARE51) and the coefficient of restitution of 0.7 (the pure ice data measured by Araoka and other, 1978) are used.

Table 5. Calculated penetration distance using different flexural strength (coefficient of restitution = 0.7)

Flexural strength [MPa]	1.0	0.8	0.7	0.5	0.3
Average [m]	5.87	7.73	8.84	12.4	16.1

Table 6. Calculated penetration distance using different coefficient of restitution (flexural strength = 0.5 MPa)

Restitution	1.0	0.8	0.6	0.4	0.3
Average [m]	12.7	12.6	12.1	12.1	12.0

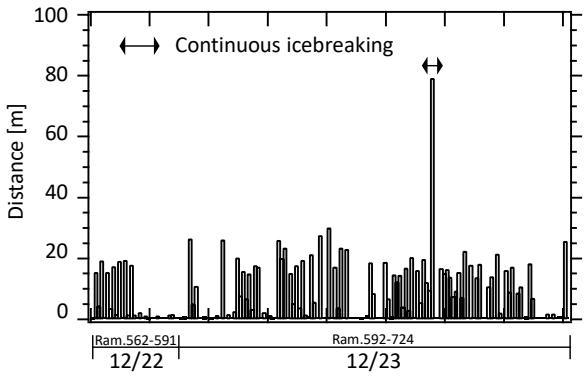

Fig. 7 Calculated penetration distance on December 22 and 23, 2013 (Area 01, Ram. No. 562–724)

4.2 Comparison of penetration distance

Fig. 7 portrays the calculated penetration distance for Area 01. Fig. 8 shows the calculated penetration distance for Area 02 and Area 03. The iterative calculation of ship ramming is ended when 10 consecutive ship rams are continued. For Area 01(2013/12/22–23), the calculated penetration distance of one ship's ram in the heavy ice condition (Fig. 7) is greater than the measured ones (Fig. 1). Some calculated penetration distances, however, become almost zero, for which only radial cracking occurs without the ice failure (circumferential cracking).

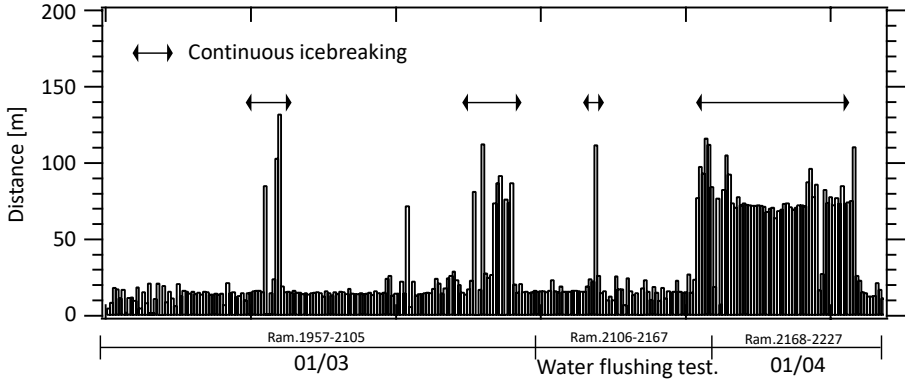

Fig. 8 Calculated penetration distance and ice thickness on Jan. 3 and 4, 2014 (Area 02 and Area 03, Ram. No. 1957–2227)

As shown in Figs. 1 and 7, distribution of the calculated penetration distance fluctuates more than that of the measured one.

For Area 02 and Area 03 (2014/1/03–04 and water flushing test), the calculated penetration distance of one ship's ram in the light ice condition (Fig. 8) is shorter than the measured ones (Fig. 2). In the calculations done for the icebreaking during Jan. 3, 2014 and in the water flushing test, the penetration distance was mostly constant: the penetration distance was about 20 m. For the calculations during Jan. 4, 2014, the continuous icebreaking continued instead of ramming icebreaking. As Figs. 2 and 8 show, the calculated distribution of the penetration distance was apparently more stable than the measured one.

Table 7 shows the total and average (standard deviation) penetration distance in one day, and the number of ship rams used for analysis of penetration distance. From Table 7, ship ram for icebreaking that was judged to be continuous icebreaking in the calculations was excluded. The calculated total penetration distance in heavy ice conditions (Area 01: 2013/12/22–23) moderately agrees with the measured values. The difference of the average penetration distance between measured data and calculated results are less than 2 m. The standard deviation of the calculated penetration distance in Area 01 is larger than that of measured one. The calculated penetration distance fluctuates more than that of the measured one in heavy ice conditions. The calculated total penetration distance in light ice conditions (Area 02 and Area 03: 2014/1/03–04 and water flashing test) was less than the measured values. The difference of the average penetration distance is around 10 m in Area 02 (2014/1/03–04), and around 17 m in Area 03 (water flushing test). The standard deviation of the calculated penetration distance in Area 02 and Area 03 are smaller than those of measured one. The calculated penetration distance was apparently more stable than the measured one in light ice conditions.

The snow thickness negatively affects the penetration distance. On the other hand, water flushing elongates the ramming distance. The measured penetration distance in the heavy ice conditions (Area 01: 2013/12/22–23) includes both effect of snow thickness and water flashing. Ice melted ponds were frequently distributed in Area 02 and Area 03 (2014/1/03–04 and water flushing test). The ice melted water reduces the friction between hull and ice, and elongates the penetration distance. In addition, the water flushing positively affects the penetration distance in Area 03. For the comparison with measured data, the calculation must include the effect of snow and water flushing. Yamauch and others (2011) investigated the snow and water flushing effect using the measured penetration distance in JARE 51. In the heavy ice condition with the ice thickness between 3 m and 4.5 m, the water flushing increased the penetration distance by 15% (around 7.5 m) regardless of snow thickness.

Table 7. Measured and calculated total, average (standard deviation) penetration distances and the number of ship rams (Top: total distance, middle: average distance, bottom: standard deviation)

Date	Measured ram [m]	Calculated ram [m]	Number of rams
2013/12/22	196	149	30
(Total, Avg.,	6.76	4.97	
Std. dev.)	3.61	7.23	
2013/12/23	991	1033	133
	7.51	7.77	
	4.26	8.69	
2014/01/03	3665	2139	136
	27.15	15.73	
	15.36	5.47	
2014/01/04	381	247	14
	27.25	17.64	
	30.81	5.59	
Water	2931	949	56
flushing test	53.30	16.95	
	22.25	5.31	

The penetration distance is strongly affected by the snow and water flushing. However calculations do not include effects of snow and the water flushing. For the calculations, the ice thickness and the mechanical properties of sea ice were assumed to be constant even when the real ship–ice conditions during ship ram were different. Only local ice crushing and global bending failure are included in the calculations as the icebreaking phenomena of the ship ramming. The propeller–ice interactions occurs normally in actual ship ramming, which reduces the propeller thrust, but they are not included in the calculations. Those problems are anticipated as reasons for the discrepancy between the calculated and measured values. They must be investigated and include in the calculation. The measured ship position is accurate to around 10 m in GPS. For the strict comparison, the more accurate data from the GPS data is needed.

4. Conclusions

This paper described the distributions of ice thickness and penetration distance of full-scale data. The calculation method of the penetration distance was proposed. In the calculations, the icebreaking by ship ram occurs by local crushing on the ice edge and the bending failure of the plate ice. The calculated penetration distance was compared with full-scale data for verification of the proposed method. The calculated penetration distance in heavy ice conditions (Area 01) moderately agrees with the measured values. Under light ice conditions (Area 02 and Area 03), the penetration distance of the calculations was shorter than those of measurements. From these results, the proposed method using bending failure as the breaking criterion in ship ramming can demonstrate the ice breaking of ship ram. However, the quantitative differences of the penetration distance between the measured data and the calculated results were shown. These discrepancies are expected to occur because of the neglect of the effects of water flushing, ice surface conditions such as snow and ice melted ponds in the calculations. Those effects must be included in calculations because the penetration distance is sensitive to ice thickness, snow thickness, and water flushing. The mechanical properties of sea ice, ship steering, cargo conditions, and so on also affect the penetration distance. To find the main contribution to the penetration distance from among them, the detailed investigation using the additional measurement data and the calculations should be done.

Acknowledgements

Authors would like to thank members of the 55th Japanese Antarctic Research Expedition and crew of Japanese icebreaker *Shirase* for great support in field tests and measurements in Antarctic sea ice. We also acknowledge the Antarctic Research Support Section, Ministry of Defense, for their permission to publish this work.

REFERENCES

Araoka. K., and Maeno. N. (1978) Measurements of Restitution Coefficients of Ice, Low Temperature Science, **A**, **36**, 55-65 (in Japanese).

Blanchet, B., H. R. Kivisid and J. Grinstead (1990): Equations for local ice energy dissipations during ship ramming. *Cold Region Science and Technology*, **18**, 101-115.

Daley, C. G. and K. Riska (1990): Review of Ship–ice Interaction Mechanics, *Report from Finnish–Canadian Joint Research Project No. 5 "Ship Interaction With Actual Ice Conditions" Interim Report on Task 1A*. Helsinki, Finland: Helsinki University of Technology.

Daley, C. (1999): Energy based ice collision forces, *Proc. of the 15th International Conference on Port and Ocean Engineering under Arctic Conditions*, **1**, 23-27.

Frederking, R (2003): Determination of Ice Pressure from Ship Transits in Ice, *Proceeding of the 13 International Offshore and Polar Engineering Conference*, **1**, 484-488.

Frederking, R and Ritch, R. (2009): The nature of the process pressure-area relation from CCGS Terry Fox berg bit impacts, *Proc. of the 19th International Offshore and Polar Engineering Conference*, 608-613.

Kishi, S. and Y. Kawashima (1997): Ramming Performance of the Patrol Icebreaker "PM TESHIO" in Full Scale and Model Scale, *Proc. of OMAE/POAC Joint Conf.*, **4**, 233-238.

Kujala, P. (1994): On the Statistics of Ice Loads on Ship Hull in Baltic, Mechanical Engineering Series, 116, Ship Laboratory, Helsinki University of Technology, Finland.

Nozawa, K. (2006): Sea ice Engineering: Seizando-Shoten Publishing Co. Ltd. Japan, 259-264 (in Japanese).

Ringsberg, J. W., M. Broman and P. Nordqvist (2014): Development of a Model for Global Response of Ship Hull during Ramming of Heavy Ice Features, *Proc. of the ASME 2014 33rd International Conference on OMAE*, OMAE2014-23186.

Sawamura, J., K. Riska and T. Moan (2008): Finite Element Analysis of Fluid–Ice Interaction during Ice Bending. *Proc. of 19th IAHR International Symposium on Ice*, 191-132.

Sawamura, J., K. Riska and T. Moan (2009): Numerical Simulation of Breaking Pattern in Level Ice at Ship's Bow, *Proc. of the 19th International Offshore and Polar Engineering Conference*, 600-607.

Sawamura, J. (2016): Ship–ice Interaction in Antarctic Sea. *Proc. of 23nd IAHR International Symposium on Ice*, USB.

Takahashi, Y., H. Yamaguchi and 3 others (2019): Turning features of an icebreaker during ramming operations: a case study. *Okhotsk Sea and Polar Oceans Research*, **3**, 13-19

Yamauchi, Y. and S. Mizuno (2009): Study on improvement in ramming performance of Antarctic icebreaker. *Proc. of the 19th International Offshore and Polar Engineering Conference*, 629-635.

Yamauchi, Y., S. Mizuno and H. Tsukuda (2011): The icebreaking performance of SHIRASE in the maiden Antarctic voyage. *Proc. of the 21st International Offshore and Polar Engineering Conference*. 1093-1099.

Okhotsk Sea and Polar Oceans Research 4 (2020) 18-22

Article

Arctic Meteorological and Geographical Observations on Dutch Whaling Vessels in 1758, 1759 and 1760

Gaston R. DEMARÉE[1], Yoshio TAGAMI[2], Pascal MAILIER[1], Astrid E. J. OGILVIE[3,4] and Takehiko MIKAMI[5]

[1]*Royal Meteorological Institute of Belgium, Brussels, Belgium*
[2]*Faculty of Human Development, University of Toyama, Toyama, Japan*
[3]*Stefansson Arctic Institute, Akureyri, Iceland*
[4]*Institute of Arctic and Alpine Research, University of Colorado Boulder, Colorado, U.S.A.*
[5]*Department of Geography, Tokyo Metropolitan University, Hachioji, Tokyo, Japan*

(Received September 26, 2019; Revised manuscript accepted December 3, 2019)

Abstract

Whaling and herring fisheries constituted major economic activities during the Dutch Golden Age (1600-1800). Whaling, in particular, contributed to the exploration of the Arctic. The focus of this paper is the analysis of five short published texts written by Pieter Cramer (1721-1776) that provide mid-18th century meteorological information as well as some observations on Arctic climate during summer season whaling in Greenland and Davis Strait.

Key words: Dutch whaling, meteorological and geographical observations, Greenland, Davis Strait

1. Dutch Whaling in the Arctic and Pieter Cramer

Pieter Cramer (1721-1776) was a wealthy Dutch merchant dealing in wool and Spanish linen in Amsterdam. He was extremely interested in natural history and assembled an extensive collection that included seashells, fossils and insects of all orders. Although he is mainly known as an entomologist his interests and capabilities were far-reaching. In 1770 he was elected Director of the Zealand Society, a scientific society located in Flushing, in the Dutch province of Zealand (*Verhandelingen uitgegeven door het Zeeuwsch Genootschap,* 1771). He was a member of *Concordia et Libertate*, a general cultural society founded in Amsterdam in 1748. His name is mentioned as Assessor in the list of Directors of *Concordia et Libertate* in the years 1762, 1763, 1764, 1765, 1767, 1768, 1771 and 1772. As a member of the society, he lectured on minerals, on rhizoliths, on electrical experiments, and on the law of accelerating motion. Cramer's main work *De uytlandsche kapellen* ("The Exotic Butterflies") was dedicated to *Concordia et Libertate*. In 4 volumes, more than 1650 butterflies from Asia, Africa and America are shown according to their actual size, are coloured by hand and described according to the Linnaeus classification system.

Pieter Cramer ordered that meteorological and geographical observations be made on board Dutch whaling vessels in Greenlandic and Davis Strait waters during the summers of 1758, 1759 and 1760. Thus he combined his situation as a wealthy merchant and Director of whaling vessels with his interest in Dutch scientific and cultural societies. Consequently, Pieter Cramer authored five noteworthy short texts containing the collected Arctic information. The context here is that one or more ships belonging to Cramer took part in whaling expeditions around 1760. Whaling in Davis Strait was dominated by the Dutch in the 18th century. Van Sante (1770) lists Pieter Cramer, sometimes written as Pieter Kramer, as Director of the Greenland whaling in 1756 and as a Director of the Davis Strait whaling in 1769. His *Commandeur* (Captain) for the years 1756 to 1761 for the Greenland whaling was Pieter Wagenaar while Herman Pronk was his *Commandeur* for the years 1769 and 1770 for the Davis Strait whaling. Cramer asked *Commandeurs* to carry out meteorological and geographical observations during the whaling expeditions to Davis Strait and other regions of the Greenland seas.

Cramer´s texts containing such information were published in the *Verhandelingen uitgegeeven door de Hollandsche Maatschappye der Weetenschappen, te Haarlem* ("Treatises published by the Dutch Society of Sciences, in Haarlem"). The "Dutch Society of Sciences" was the major scientific society in the Netherlands in the 18th century. The texts are labeled as *Berichten aan de Maatschappye gegeeven* ("Accounts submitted to the Society") and are distinguished from the *Verhandelingen*. However, besides the name of the author of the paper no information on the Directors, the *Commandeurs* or the ship names are given. In order to try to identify this missing information a search has been made through eighteenth-century Dutch literature

including newspapers, magazines and books.

Dutch newspapers such as the *Amsterdamse courant,* the *Oprechte Haerlemsche courant,* the *Middelburgsche courant* and the monthly magazine the *Maandelykse Nederlandsche Mercurius* ("Monthly Dutch Mercurius") inform their readers of the departure and arrival of whaling vessels to Greenland and to Davis Strait. Usually, the name of the ship, the wind direction at Texel, the catch and the load is mentioned which confirms and/or completes the information. Examples of this type of information are given below.

"Amsterdam, 12 April 1758. … on 11 April are departed … Pieter Wagenaar, … all to Greenland." - "Amsterdam, 31 July 1758 ... arrived at Texel on 29 July … and Pieter Wagenaar, empty, from Greenland; the wind Northerly."

The communication in the '*Treatises of the Dutch Society*' mentions 15 April 1758 as the departure day and 21 July 1758 as arrival day.

"Texel, 26 April 1759. … On 23 April 1759 are sailed out … '*t Huis Daalbende* ("The Daalbende House"), Pieter Wagenaar, …, all to Greenland; the wind North N. East."

Pieter Cramer´s father, Johann Jacob Cramer, was born in 1663 in "House Dalbenden", near Urft, in the Eifel (in the German state of North Rhine-Westphalia). It is of interest to note that this ship of Pieter Cramer, '*t Huis Daalbende*, was clearly named for his father´s house (Roepke, 1956).

On the list of Dutch Greenland ships arriving in the harbours of the country Pieter Wagenaar is included as *Commandeur* on '*t Huys Daalbende* arriving on 21 August 1759, with 1 whale and 30 barrels (*Maandelykse Nederlandsche Mercurius*, November 1759, pp. 187-190). According to Cramer's paper the ship left on 7 April 1759 and returned on 26 July 1759. It may therefore be questioned if it deals with the same ship sailing to Greenland.

"Texel, 21 April 21 1760. … On 20 April 1760 are sailed out, all to Greenland, … *'t Huis te Daalbende*, Pieter Wagenaar, ...: the wind S. West."

"Amsterdam, 20 August 1760. On 18 August arrived at Texel … and Pieter Wagenaar, with 1 whale, 40 quarteel, the wind S.W."

According to Pieter Cramer's article the sailing out started on 15 April 1760 and the ship returned at 15 August 1760.

It is noted that, in general, the first and last days of the meteorological and geographical observations in the published papers regarding the ship left Texel or would arrive at Texel do not correspond to the dates mentioned in the Dutch newspapers or monthly magazine. Furthermore, the observations usually start when the ship has left the *Rede van Texel*, a roadstead off the Dutch island of Texel near the village Oudeschild. Similarly, the observations end before the ship arrives. The geographical coordinates of the *Rede van Texel* are: 53° 03' N, 4° 51' E.

This complicates the identification of the whaling vessel sailing in 1759 and in 1760 to Davis Strait as Pieter Cramer is not mentioned for whaling in Davis Strait in those years. It may be speculated that the *Commandeur* was Hendrik Pronk on the *Maria Christina* as Pronk is Cramer's *Commandeur* for the Greenland whaling, 1762 to 1771.

"Texel, 30 March 1759. On 26 March sailed the *Maria Christina*, Hendrik Pronk, to Davis Strait, the wind W. S. West." - "Amsterdam, 8 August 1759. ... arrived at Texel on 7 August … Hendrik Pronk, 3 whales, 136 q., the wind W. Northwest." - "Texel, 14 March 1760. On the 13th are sailed … the *Maria Christina*, Hendrik Pronk, all to the Davis Strait, the wind S. West." - "Amsterdam, 18 August 1760. On 17 August did arrive at Texel … Hendrik Pronk, 3 whales and 140 quarteel of whale-oil from Davis Strait."

2. Meteorological and Geographical Observations

Meteorological observations on board the whaling ships were generally carried out twice a day at 7 am and at noon. However, for the year 1758 these observations were taken at 7 am and at 7 pm. The thermometer with which these observations were made was a Fahrenheit scaled thermometer. Following the instructions of Pieter Cramer, the thermometer was hung in the corridor to the cabin in which the *Commandeur* slept. The reason for this somewhat sheltered location is that Cramer had experienced that his metal clock broke into pieces the year before as a result of the extreme frost and he also did not want any of the crew to accidentally damage the thermometer (Cramer, 1761, Berichten, 6(1), p. 380)

The following meteorological observations were carried out: air temperature, wind direction using 16 or 32 cardinal directions, and a description of the state of the sky, including the wind strength. The state of the sky and the wind strength are expressed in Dutch 18th century nautical terms. The geographical observations are limited to the latitude (degrees, minutes) The longitudinal observations are only given for the whaling vessel sailing to Davis Strait in 1759. These latitudinal observations are expressed using the zero meridian at Pico de Teide on the Canary Islands and are expressed from 0° to 360° East. However, due to the technical problems inherent in early longitudinal observations longitude was only observed when the whaling vessel was in the North Sea, crossing the Atlantic Ocean and entering Davis Strait and on the same return journey. On its return travel the whaling vessel crossed the North Atlantic south of Iceland and the Faroe Islands, sailed between the Shetland islands and the Orkney islands to the North Sea.

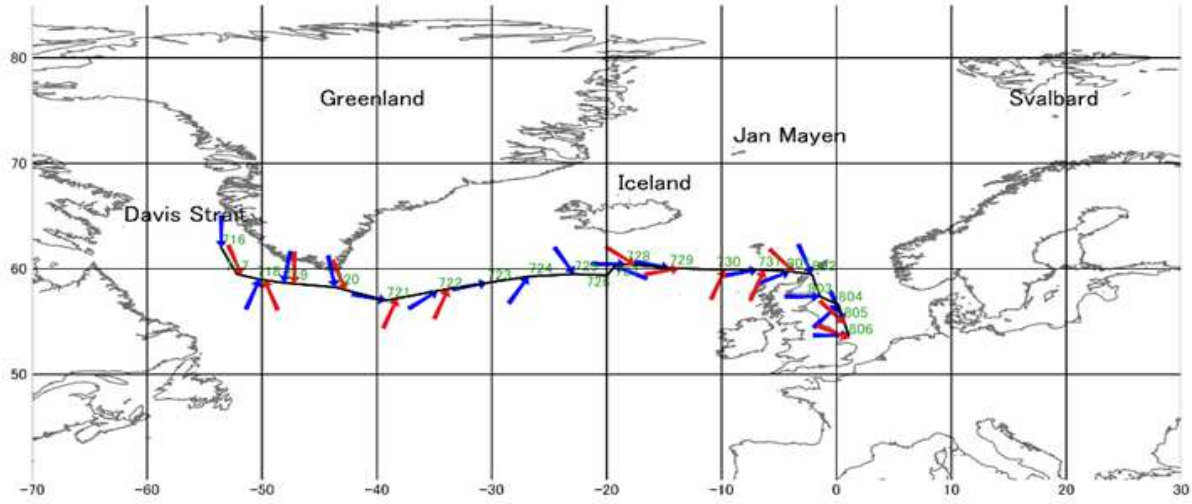

Fig. 1 Return ship-route and wind directions at 7 am (blue arrow) and at 12 noon (red arrow) of Pieter Cramer's whaling ship to Davis Strait in 1759.

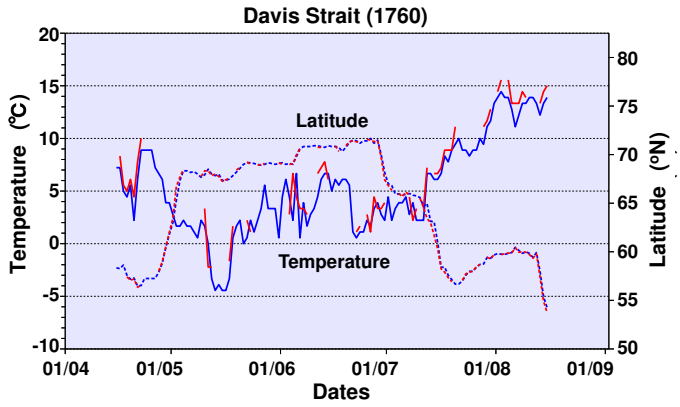

Fig. 2 Temperature observations at 7 am (full line blue) and at noon (full line red) and the latitude observations at 7 am (dashed line blue) and at 12 noon (dashed line red) of Pieter Cramer's whaling ship to Davis Strait in 1760.

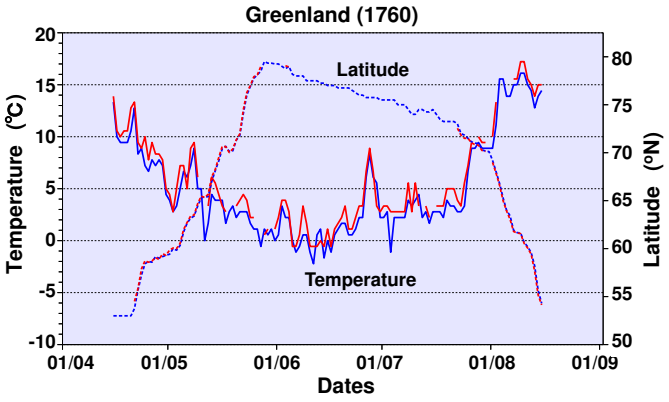

Fig. 3 Temperature observations at 7 am (full line blue) and at noon (full line red) and the latitude observations at 7 am (dashed line blue) and at 12 noon (dashed line red) of Pieter Cramer's whaling ship to Greenland in 1760.

Figures 2 and 3 represent the twice-a-day temperature observations of the Dutch whaling ships to Davis Strait and to Greenland in 1760 based upon the data in Pieter Cramer's texts. On 28 May 1760, the latitude of 79° 30' N was reached. However, on the whaling expedition to Greenland in 1758 the latitude of 80° N was maintained from 26 June to 4 July 1758. The explorer William Scoresby reached 81° 30' N near Svalbard on the ship *Resolution* on 23rd May 1806 (Takahashi, 2019). From 10 May 1760 to 24 June 1760 the temperature varied in the order of 30° to 40° F. However, on the whaling expedition in 1758 to Greenland the temperature fell below 30° F for the period 26 April 1758 to 29 May 1758. A warmer *vs.* a colder summer year in the North Atlantic?

As there are no longitude observations when whaling, it is interesting to compare the latitude observations in Davis Strait with locations known through Dutch whaling history. Cape Farewell, the most southern tip of Greenland, is at 59° 46' N. In Pieter Cramer's texts, the most northerly location in Davis strait in 1759 was 71° 30' N and in 1760 was 71° 40' N. This is slightly below the location 72° 47' N of Upernavik but near the well-known locations of Dutch whaling at Rode Bay [Ogaatsuk], Disko Bay, Egedesminde [Aasiaat] and Jacobshavn [Ilulissat]. Similarly, the most northerly location of the Greenland whaling was 80° N in 1758, 78° 30' N in 1759 and 79° 30' in 1760; the location of the island Jan Mayen (Norway) is 70° 59' N and Smeerenburg on Svalbard is 79° 44' N.

In the context of latitudes and whaling, it is interesting to plot the temperature observations *vs.* the latitude observations as registered in Pieter Cramer's 5 short texts dealing with the years 1758, 1759 and 1760 in the eastern Greenland seas region and with the years 1759 and 1760 in Davis Strait. In Figures 4 and 5 the temperature observations are represented as coloured

dots per year in function of the latitude observations. The start and return of the whaling vessel is shown in the top left quarter of the figure. These dots represent relatively mild temperatures in spring and summer during the crossing of the North Sea and of the Atlantic Ocean. For the Davis Strait whaling, the vertical group of red dots around the latitude 67° N seem to indicate a colder period in the summer of the year 1759. In the Greenland whaling the dots remain between 5° C and 15° C for latitudes approximately below 67° N. They drop to between 0° C and 10° C for latitudes between 67° N and 75° N, and for latitudes between 75° N and 80° N the temperature ranges between -10° C and nearly +10° C, depending on the daily weather conditions.

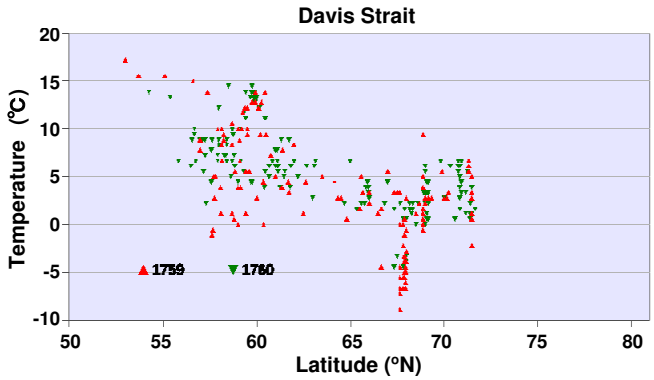

Fig. 4 Graph showing the temperature observations in terms of latitude observations for Pieter Cramer's whaling vessels in 1759 (red colour) and in 1760 (green colour) in Davis Strait whaling.

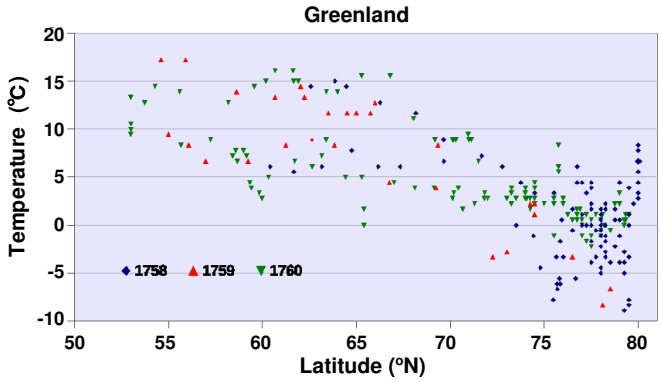

Fig. 5 Graph showing the temperature observations in terms of latitude observations for Pieter Cramer's whaling vessels in 1758 (black colour), in 1759 (red colour) and in 1760 (green colour) in Greenland whaling.

The graph in figure 5 representing the temperature observations in terms of the latitude in the Greenland whaling shows three different groups: the numerous dots when whaling at latitudes between 70° N and 80° N, and the dots representing the thermal conditions when sailing to or sailing from the whaling areas. These dots clearly indicate the change of temperature with latitude and could be represented by a straight regression line with different slopes due to the different seasons when sailing.

The groups of dots on a vertical line may refer to chasing a whale or a group of whales, to the cutting of a caught whale or to the prolonged stay on one of the whaling harbours such as Disco Bay, Rode Bay in Davis Strait, or Jan Mayen or Smeerenburg in the Greenland whaling. It is also possible that the whaling vessel got caught in drift ice at northern latitudes and remained immobile for a short time.

3. Anton Rolandson Martin's Meteorological and Geographical Observations in the Arctic

Carl Linnaeus, the renowned Swedish botanist and professor at Uppsala University, suggested that his student, Anton Rolandson Martin (1729-1786) travel with a whaler to the Arctic. This was *De Visser* ("The Fisherman"), a small fishing boat, in Dutch a *hoeker*, ("hooker"). The vessel was owned by the Swedish Gothenburg-based Greenland Company with the Dutchman Jan Dircks Claessen as Captain and a mixed Dutch and Swedish crew.

During the journey Martin made systematic weather observations. Three times a day: at 6 o'clock in the morning, at noon and at midnight, he carried out temperature observations, recorded the dominating wind direction and the weather of the day. Latitude was determined at noon by measuring the sun's height above the horizon. The vessel departed Gothenburg on 17 April 1758 and reached the same harbour on 24 July 1758. Martin's Arctic observations together with Pieter Cramer's ones are among the first explorations of the meteorology of Polar Oceans (Martin, 1758a, 1758b, Hagström, 2018).

4. Conclusion

The meteorological observations, together with latitudinal information carried out aboard 5 Dutch whaling vessels in the years 1758, 1759 and 1760 are among the earliest ones in the Polar oceans. The short papers containing this information are authored by Pieter Cramer, a merchant from Amsterdam. The name of the Director, the *Commandeur* and of the vessels are not specified in these short texts but contemporaneous 18th century newspapers, journals and published material have provided insights into these questions.

Acknowledgements

The lead-author is grateful to Diederick Wildeman, National Maritime Museum at Amsterdam, for having provided useful information on Dutch whaling. The authors acknowledge two anonymous reviewers for their constructive remarks, in particular reviewer F2 for his suggestion to search for the meteorological observations of Anton Richardson Martin. Astrid Ogilvie acknowledges Nordforsk award 76654 *Arctic Climate Predictions: Pathways to Resilient, Sustainable Societies (ARCPATH)*.

References

Bruijn, J.R. en Hacquebord, L. (2019) Een zee van traan: vier eeuwen Nederlandse walvisvaart 1612-1964 [A sea of whale-oil: 1612-1924]. *Zutphen: Walburg Pers* (in Dutch).

Cramer, Pieter (1761) Waarneemingen gedaan op de Groenlandse Uit en Thuis Reis, in den Jaare 1758 - Waarneemingen gedaan op de Groenlandse Uit en Thuis Reis, in den Jaare 1759 [Observations made on the travel to and from Greenland in the year 1758, ... in the year 1759]. Gezonden aan de Maatschappye door Pieter Cramer. *Verhandelingen uitgegeven door de Hollandse Maatschappye der Weetenschappen te Haarlem*, Berichten, **6**(1), 374-380, 381-387 (in Dutch).

Cramer, Pieter (1761) Waarneemingen gedaan op de Straat Davids Uit en Thuis Reis, in den Jaare 1759 [Observations made on the travel to and from Davis Strait in the year 1759]. Gezonden aan de Maatschappye door Pieter Cramer. *Verhandelingen uitgegeven door de Hollandse Maatschappye der Weetenschappen te Haarlem*, Berichten, **6**(1), 388-396 (in Dutch).

Cramer, Pieter (1762) Waarneemingen gedaan op de Groenlandse Uit en Thuis Reis, in den Jaare 1760 [Observations made on the travel to and from Greenland in the year 1760]. Gezonden aan de Maatschappye door Pieter Cramer. *Verhandelingen uitgegeven door de Hollandse Maatschappye der Weetenschappen te Haarlem*, Berichten, **6**(2), 70-77 (in Dutch).

Cramer, P. (1762) Waarneemingen gedaan op de Straatdavids Uit en Thuis Reis in den Jaare 1760 [Observations made on the travel to and from Davis Strait in the year 1760]. Gezonden aan de Maatschappye door Pieter Cramer. *Verhandelingen uitgegeven door de Hollandse Maatschappye der Weetenschappen te Haarlem*, Berichten, **6**(2), 78-86 (in Dutch).

Cramer, P. (1779-1782) De Uitlandsche kapellen voorkomende in de drie waereld-deelen Asia, Africa en America [The exotic Butterflies occurring in the three Continents Asia, Africa and America], by *een verzameld en beschreeven door den Heer Pieter Cramer, ..., Amsterdam, S.J. Baalde, Utrecht, B. Wild* (in Dutch).

Gemeente Amsterdam, City Archive, No. 9, Archief van het Genootschap Concordia et libertate (in Dutch). https://archief.amsterdam/inventarissen/inventaris/9.nl.html

Hagström, J. (2018) Where Swedish polar research began: The Linnaean apostle Anton Rolandson Martin's voyage to Spitsbergen in 1758. *Polar Record*, 54(1), 36-42.

Martin, A.R. (1758a) Meteorologiska observationer, gjorde på en Resa til Spits-bärgen [Meteorological observations made on a journey to Spitsbergen]. *Kongliga Vetenskaps-Academiens handlingar För Månaderna October, November, December År 1758*, 307-315 (in Swedish).

Martin, A.R. (1758b) Witterungsbeobachtungen auf eine Reise nach Sptizbergen [Weather observations on a journey to Spitsbergen]. *Der Königl. Schwedischen Akademie der Wissenschaften Abhandlungen aus der Naturlehre, Haushaltungskunst und Mechanik, auf das Jahr 1758*. 20. Band, Hamburg und Leipzig, 292-300 (in German).

Roepke, W. (1956) Enkele aantekeningen over het werk van Pieter Cramer en over zijn persoon [Some notes about the work of Pieter Cramer and about his person]. *Entomologische Berichten*, **16**, 25-28 (in Dutch).

Sante, G. van (1770) *Alphabethische naam-lyst van alle de Groenlandsche en Straat-Davissche commandeurs, die zedert het jaar 1700 op Groenland, en zedert het jaar 1719 op de Straat-Davis, voor Holland en andere Provincien hebben gevaaren ... [Alphabetical name-list of all Greenland and Davis Strait Captains who have sailed for Holland and other Provinces since the year 1700 on Greenland and since 1717 on Davis Strait]*, Haarlem (in Dutch).

Takahashi, S. (2019) Arctic exploration history and climatic change. *Proceedings of the 34th International Symposium on Okhotsk Sea & Sea Ice, Mombetsu, Japan*, **34**, 401-404.

Verhandelingen uitgegeven door het Zeeuwsch Genootschap der Wetenschappen te Vlissingen (1771), **2**, XLVII (in Dutch).

Summary in Japanese

和文要約

1760 年前後のオランダ捕鯨船による北極域の気象学的・地理学的観測

Gaston R. DEMARÉE[1], 田上善夫[2], Pascal MAILIER[1], Astrid E.J. OGILVIE[3,4], 三上岳彦[5]

[1] ベルギー王立気象研究所, [2] 富山大学, [3] ステファンソン北極研究所, [4] コロラド大学ボルダー校, [5] 首都大学東京

捕鯨とニシン漁業は、オランダ黄金時代（1600−1800）の主要な経済活動の担い手であった。とくに捕鯨は北極圏の探査に貢献した。 5 編の短報が出版され、グリーンランドとデービス海峡における夏季捕鯨中の北極気候下での限られた地理的観察とともに 18 世紀半ばの気象観測の状況が明らかになった。さらに、これらの短報に記載されている船長、指揮官、船の名前の特定が試みられている。

Submission Information for OSPOR

Reviewing processes of OSPOR

1) When manuscripts have been received by the Editor-in-Chief, an acknowledgement of receipt will be sent to the author(s) by e-mail. The Editor-in-Chief chooses an editor to handle the manuscript review.
2) The submitted manuscript will be subjected to screening review for its scope, novelty, completeness, English level, and conformation to the OSPOR policy. A manuscript not passing the screening review will immediately be returned to the authors.
3) The editor in charge will select expert reviewers to evaluate the manuscript.
4) As to results of review, if the editor decides that the paper needs revision by the author(s), the manuscript will be returned to the author(s) for revision.
5) Manuscripts returned to author(s) for revision should be resubmitted promptly. If the revision cannot be finished within a month, the manuscript will be regarded as having been withdrawn.
6) The Editor-in-Chief will finally decide whether to accept the manuscript for publication.

Paper Submission

Submission Guideline

All manuscripts should be submitted in digital format (PDF or WORD) with the OSPOR submission sheets (PDF or WORD, offered from OSPOR) by email to the OSPOR Editorial Board

OSPOR Editorial Board

Polar Oceans Research Association (OSPORA)
Address: Kaiyo Koryukan, 1 Kaiyo Koen, Mombetsu, Hokkaido 094-0031 Japan
E-mail: momsys@o-tower.co.jp
Phone : +81-158-26-2810 (Japan 0158-26-2810)
Fax: +81-158-26-2812 (Japan 0158-26-2812)

Publication Charge*

Authors of their institutions are requested to pay the publication charge according to the following rate when paper is accepted. The maximum pages are 6 pages.

1,500 Yen / page within the maximum pages
3,000 Yen / page over the maximum pages (Excess charge)

Copyright

Copyright for an article submitted to OSPOR is transferred to OSPORA when the article is published in OSPOR in any form.

Preparation of manuscripts

The manuscript should be formatted in the form of OSPOR template offered from the OSPORA office, which satisfies the following requirements. The maximum pages in printing style are **6 pages**.

1) Text
   a) The manuscript should be in the international size A4 in camera-ready style according to the form of OSPOR template.
   b) The first page should include: the title, the author(s) name(s) and their affiliations. If possible, a Japanese translation of the title and the name(s) of the author(s) should be provided in the end of manuscript. If they are not, the translation will be undertaken by the OSPOR editorial board.
   c) An abstract not exceeding 250 words must be provided.
   d) Up to five keywords that describe the content for indexing purposes must be provided.

2) References

a) A list of cited references should be arranged alphabetically. Journal abbreviations are better to use, but when the abbreviation is not known, the full title of the journal should be used in the list.

In the case of many authors, the author name can be written in short as below.

Kawamura, K., F. Parennin and 16 others (2007): Northern hemisphere forcing of climatic cycles in Antarctica over the past 360,000 years. *Nature*, **448**, 912-916.

b) References in the text will include the name(s) of the author(s), followed by the year of publication in parentheses, *e.g.* (Clark, 2003), (Li and Sturm, 2002), (Harrison and others, 2001).

3) Units

Numerical units should conform to the International System (SI).
Units should be in the form as kg m^{-3} not as kg/m^3.

4) Tables

A title and a short explanation should be located on the top of table.
They should be referred to in the text.

5) Figures

a) All Figures (illustrations and photographs) should be numbered consecutively.
b) All Figures should be of good quality and referred to in the text.
c) Figure captions should be located on the bottom of the Figures.

6) Submission sheet

When you submit a manuscript for OSPOR, check the manuscript with a submission sheet, and submit it with your manuscript.
http://okhotsk-mombetsu.jp/okhsympo/artical-J/submiss-sheetJ.html

7) File name

A file name for manuscript is better to be as
Name_OSPOR_Article (Review)_(20yymmdd).pdf (docx)

8) More information

For more information about manuscript instruction, please ask to OSPORA office or see OSPORA home page in http://okhotsk-mombetsu.jp/okhsympo/top-index.html

Recent information*

Resent information can be get from the following URL.

General Information: http://okhotsk-mombetsu.jp/okhsympo/artical-J/Info-artical.html
Instruction: http://okhotsk-mombetsu.jp/okhsympo/artical-J/Instruction-J.html
Template: http://okhotsk-mombetsu.jp/okhsympo/artical-J/Template-J.html
Submission Sheet: http://okhotsk-mombetsu.jp/okhsympo/artical-J/submiss-sheetJ.html

Okhotsk Sea and Polar Oceans Research, Vol. 4 (2020, February)

Published by the Okhotsk Sea and Polar Oceans Research Association (OSPORA),
Mombetsu City, Hokkaido, Japan

Executive Committee of OSPORA:

Chairman: Shuhei Takahashi (Okhotsk Sea Ice Museum of Hokkaido, Director)

Secretariat: Eriko Uematsu

Address: Kaiyo Koryukan, 1 Kaiyo Koen, Mombetsu, Hokkaido 094-0031 Japan

E-mail: momsys@o-tower.co.jp

Phone : +81-158-26-2810 (Japan 0158-26-2810)

Fax: +81-158-26-2812 (Japan 0158-26-2812)

http://www.o-tower.co.jp/okhsympo/top-index.html

Okhotsk Sea and Polar Oceans Research

Published by the Okhotsk Sea and Polar Oceans Research Association (OSPORA)
Mombetsu City, Hokkaido, Japan

Vol. 4